COMPOSITION-PROCESSING-PROPERTY RELATIONSHIPS OF 3D-PRINTED GRAPHENE-EGAIN-POLY(ETYLENE OXIDE) COMPOSITES

By

RUCHIRA TANDEL

A dissertation submitted in partial fulfillment of
the requirements for the degree of

DOCTOR OF PHILOSOPHY

WASHINGTON STATE UNIVERSITY
School of Mechanical and Materials Engineering

DECEMBER 2023

To the Faculty of Washington State University:

The members of the Committee appointed to examine the dissertation of RUCHIRA TANDEL find it satisfactory and recommend that it be accepted.

Arda Gozen, Ph.D., Chair

Roland Chen, Ph.D.

Scott Beckman, Ph.D.

ACKNOWLEDGMENT

I would like to express my deepest gratitude to the following individuals without whom the completion of this dissertation would not have been possible. I am profoundly grateful to my advisor, Dr. Arda Gozen, for his unwavering support, guidance and mentorship throughout this journey. His expertise, patience and encouragement have been invaluable in shaping this research. To my family, Deepanjali (mumma), Prabhakar (pappa) and Priyanka (dida), your constant love and support have been my anchor. Your sacrifices and understanding during this demanding period of my life are deeply appreciated. My friend, Praveer, for his constant help, support and care whenever and wherever required. I am grateful to my friends and peers, Charudatt, Sanket, Boulder, Kimberley, Mamatha, Kimberlee, Caitlin and Steve, who shared their time and experience, making this journey more memorable and enjoyable. I want to express gratitude to my love, Pankaj, for your belief in me and your presence by my side have been my greatest blessings. Completing this dissertation has been a challenging yet rewarding endeavor and I am humbled by the support and encouragement I have received along the way. Thank you all for being a part of this academic journey.

COMPOSITION-PROCESSING-PROPERTY RELATIONSHIPS OF 3D PRINTED GRAPHENE-EGAIN-POLY(ETYLENE OXIDE) COMPOSITES

Abstract

by Ruchira Tandel, Ph.D.
Washington State University
December 2023

Chair: Arda Gozen

Direct Ink Writing (DIW) is an extrusion-based additive manufacturing method that involves the deposition of inks through a nozzle in a layer-by-layer fashion. This method utilizes liquid-phase functional ink consisting of various materials among which polymer composites (PCs) are widely used. The capabilities of DIW to precisely control microstructure make it an ideal technique for harnessing the achievable properties of these materials to their fullest potential. For the effective realization of this capability in manufacturing, a thorough understanding of the material-process-property relationships and the driving mechanisms pertaining to DIW of PCs is essential. To this end, our research delves into the intricate dynamics of DIW, focusing on how various process parameters and material characteristics influence the final properties. Specifically, we examined a polymer composite ink that consists of a poly(ethylene oxide) (PEO) binder and two distinct fillers: graphene and Eutectic Gallium Indium (EGaIn). The presented approach involves studying two distinct compositional ranges and aspects of the DIW process: 1) a low-loaded formulation with 5% volumetric filler concentration to examine the

relationship between shear and extensional ink rheology and process mechanisms involving the flow and deformation of inks between the nozzle and the substrate; and 2) a high-loaded formulation with up to 15% volumetric filler concentration to investigate the mechanics of ink flow inside the nozzles, focusing specifically on wall-slip and shear deformation. For both cases, the influence of these different process mechanisms on the electrical conductivity of the printed structures has been extensively analyzed. Lastly, to achieve more precise modeling of the complex ink behavior during DIW, this thesis takes the first step by introducing a modeling framework designed to simultaneously represent shear and extensional flow behavior through non-linear viscoelastic model.

By elucidating the material-process-property relationships for DIW of PCs, this thesis informs the ink and process design for DIW towards manufacturing conductive PC structures with as-designed functional properties. It also lays the groundwork for future studies on DIW that holistically combine ink rheology, complex process mechanisms and property control through microstructural evolution.

TABLE OF CONTENTS

Page

LIST OF TABLES

Page

LIST OF FIGURES

Page

CHAPTER 1

CHAPTER 2

CHAPTER 3

APPENDIX B

Dedication

I dedicate this dissertation to my family, whose love and support have always been the pillars of this journey.

CHAPTER ONE: INTRODUCTION

Polymer composite (PC) material system synergistically combines the ideal properties of its polymer matrix and nano particle fillers like electrical, mechanical and thermal[1]–[3] properties. It makes the PCs unique and multifunctional which cannot be achieved by conventional materials. PCs with such unique properties has plausible applications in fields such as sensors & actuators, bio-implants, soft robotics and energy storage devices. These properties strongly depend on the properties of the filler particle and their organization within the composites, which is primarily driven by the method used to process these materials. The processing of such complex systems is also highly dependent upon the rheological properties of the composite constituents, which renders the polymer composite development and manufacturing a challenging task.

Conventional manufacturing methods to form functional products using solution-based processing include screen printing, solution casting, etc. The advantage of the methods is its high throughput however it has difficulties in production of complex design. Additionally, main drawback of these methods is low resolution of the final products. Most critically, these processes have limited control over the morphology of the composite constituents in the manufactured part which leads to inaccuracies with respect to desired properties.

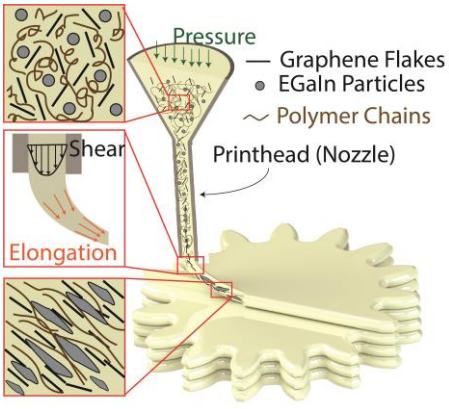

Figure 1. Direct Ink Writing of Graphene-EGaIn-Polyethylene

One of the potential ways of addressing these issues and improving the processing of PCs is Additive Manufacturing (AM). A specific AM method that is tailored well for PCs is a material extrusion-based method known as Direct ink writing (DIW)[4], [5]. DIW is a process where

feedstock ink is continuously dispensed through a nozzle with high special control and deposited on a substrate. DIW carries the capability to control the PN filler morphology filament-by-filament[6]. This precise control combined with its multi-material capability, enables DIW to generate functionally graded parts with heterogeneity ranging from macro to sub-micron scales. It has been shown to achieve high resolution manufacturing of PCs structures with deterministic filler morphologies. DIW technology has been proven in applications for the fabrication of electrodes, sensors, super capacitors, flexible electronics, and capacitive touch pads[7], [8]. To achieve these capabilities of DIW process, a strong fundamental understanding of process mechanism and its relationship with material properties is required.

Several studies have demonstrated successful processing of Gr-PCs using DIW. Particularly, inks derived from Gr-PCs possess the rheological properties favorable for the DIW process such as shear thinning, high shear yield stress and increased apparent viscosity to enable 3D printing of objects[9], [10]. It has been shown that the graphene particles align along printing direction which significantly influences the functional properties of the printed parts.

Lately, liquid metals are drawing attention for its Eutectic alloys such as EGaIn that have melting points below room temperature and its uses with soft materials for various applications. These liquid metals are encapsulated under an oxide shell which can be deformed easily, making it moldable[11]. As a room temperature liquid metal alloy, it has both high electrical & thermal[12] conductivity and ability to deform, leading to its applications in wearable electrical devices. The PCs with EGaIn fillers introduce stretchability feature which increases its flexibility and thereby opens the window for its use in making soft and stretchable devices. Novel soft and stretchable electrodes are being manufactured as wearable bio-monitors using Eg-PC[13]. Furthermore, these fillers have been shown to alter the PCs' precursor rheology in unique ways like reducing shear

viscosity and increasing viscoelasticity[9]. Interestingly, the presence of oxide shell prevents the particle to form electrical pathway when used as a filler in PC. Another promising approach is when these particles are integrated with other solid fillers like silver, graphene or gold, they contribute to increasing the electrical conductivity and shows unique properties such as reducing the shear viscosity which is unlike any other solid fillers[9]. Basically, more research on this complex material systems (i.e., including EGaIn and solid fillers) and its influence on processing and final PC properties is required.

The overarching objective of this work is to fundamentally study the material-process-property relationships for DIW of Graphene-EGaIn-Polyethylene oxide (Gr-Eg-PEO) based composites. Considering the highly complex nature of this material system, achieving this objective requires research effort in multiple different directions including rheological characterization and material modeling of the inks that are used as the DIW process feedstock and extensive experimental studies to understand the driving mechanisms of the DIW process.

During the period of this thesis work, it has been found that the particular material system of interest exhibits significantly different rheological properties and driving mechanisms associated with different aspects of the DIW process for different compositional ranges. As such, this thesis distinguishes between two compositional ranges for the PC inks investigated, referred to as low-loaded and high-loaded inks and includes two studies, presented in Chapters 2 and 3, dedicated to these two different types of materials and the associated aspects of the process. Low loaded inks include 5% of total volumetric filler concentration (Graphene flakes + EGaIn particles) while high loaded inks include 15-18% of total volumetric fillers concentration. In these studies, only viscous shear and extensional flow of these inks were considered. The final chapter presents our efforts to

model the material rheology more accurately by considering non-linear viscoelasticity. The details of these three studies are provided below:

Study (I): Composition-process-property relationships for low-loaded PC inks

In this study, we focus on characterizing low-loaded ink using under-extrusion regime. This approach enables us to explore the influence of EGaIn fillers on the composite rheology and how that influences the flow and deformation of the ink after extrusion i.e. we explore the relationship between the extensional rheology and mechanism pertaining to ink flowing between the nozzle and substrate. Additionally, we investigate the influence of EGaIn fillers on the printing resolution and electrical conductivity of the printed structure.

Study (II): Composition-process-property relationships for high-loaded PC inks

In this study, we focus on how the composition of inks and the direct ink writing (DIW) process parameters, such as nozzle size and flow rate, influence the electrical conductivity of highly loaded PC ink prints. We explored the mechanics of ink flow inside the nozzles, specifically wall-slip and shear deformation, using capillary, rotational rheometry and flow modelling to understand their effects on the microstructure and conductivity of printed parts.

Study (III): Non – linear Viscoelastic modeling of GrEgPEO Inks

The shear and extensional rheological data of the studied inks is used to model the non-linear viscoelastic behavior of the inks through various sophisticated constitutive models. These models comprehensively captured the behavior of inks under various normal and shear stresses. These models will substantially contribute to the modeling of the DIW process by increasing the complexity of the material models used in the current state of the art.

Key contributions of this work:

1. Elucidated the connections between ink extensional rheology and printability as well as functional properties for DIW of low-loaded PCs.
2. Developed an experimental and modeling framework to identify the contributions of shear flow and wall-slip during DIW.
3. Elucidated the influence of wall-slip and shear flow contributions to the ink flow on the functional properties of PC inks.
4. Revealed the unique contributions of sub-10 μm eutectic GaIn fillers to the rheology and DIW process mechanisms when included in PC inks.
5. Developed a non-linear viscoelastic modeling framework that utilizes both shear and extensional rheology data.

Contributions 1-4 has been disseminated in the form of journal articles listed below:

1. Tandel, Ruchira, and B. Arda Gozen. "Direct-Ink-writing of liquid metal-graphene-based polymer composites: Composition-processing-property relationships." *Journal of Materials Processing Technology 302 (2022): 117470.* https://doi.org/10.1016/j.jmatprotec.2021.117470.
2. Tandel, Ruchira, Sargin, Irmak, and B. Arda Gozen. " Flow Mechanisms and Their Influence on the Properties of EGaIn-Graphene-Poly(ethylene) Oxide Composites During Material Extrusion-based Additive Manufacturing." Additive Manufacturing, under review.

CHAPTER TWO: DIRECT-NK-WRITING OF LIQUID METAL-GRAPHENE-BASED POLYMER COMPOSITES: COMPOSITION-PROCESSING-PROPERTY

Tandel, Ruchira, and B. Arda Gozen. "Direct-Ink-writing of liquid metal-graphene-based polymer composites: Composition-processing-property relationships." Journal of Materials Processing Technology 302 (2022): 117470.
https://doi.org/10.1016/j.jmatprotec.2021.117470.

Originally published in *Journal of Material Processing Technology*.

Attributions:
Arda Gozen supervised the research, offered direction, and suggested experiment techniques. He clarified the results and reviewed the manuscript for edits.

1. Introduction

Polymer composites (PCs) synergistically combine the desired properties of polymers (e.g. mechanical toughness, dielectric loss) and filler particles (e.g. electrical and thermal conductivity) to yield unique bulk properties that cannot be achieved by other material systems. PCs have been utilized in a number of technologies including tissue engineering [14], energy storage [15], wearable and conformable electronics [16], and biochemical sensing [17]. These unique properties are strong functions of the filler particle properties and their organization within the composites, which is primarily driven by the methods used to process these materials. The processing of such complex systems is also highly dependent upon the rheological properties of the composite constituents, which renders the PC development and manufacturing a challenging task. As such, there is an emerging demand for research focusing on new material systems and the unique processing methods to unlock the new properties and functionalities that can be achieved using PCs.

Among the most common fillers used in PCs are carbon-based, such as carbon nanotubes [18], carbon black [19], graphene [20], and graphite [21] for thermal and electrical conductivity improvement. Other examples include ceramics [22] and clay nanocomposites such as silica organoclay [23] or metallic fillers [24]. A new type of filler that have recently drawn attention are the ones derived from eutectic alloys that have melting points below room temperature including Eutectic Gallium-Indium (EGaIn) or Galinstan. These liquid metal particles are encapsulated by their oxide skin which render them soft and deformable unlike conventional rigid fillers. Addition of EGaIn fillers to PCs has been shown to improve their toughness and tear resistance significantly [25] by increasing the energy dissipation due to the deformability of liquid metal inclusions under

loading. It has also been demonstrated that the addition of EGaIn enhances thermal and electrical conductivity of elastomeric parts [26]–[28]. Interestingly, the presence of the nanometric oxide skin prevents these particles from forming conductive pathways even above their percolation thresholds [29]. Accordingly, unlike many metal nanoparticle additives, PCs with EGaIn additives are not inherently electrically conductive, unless they go through a mechanical sintering process to rupture the particles and form conductive pathways [30]. EGaIn fillers can still make contributions to composites' electrical conductivity when used in conjunction with other rigid conductive fillers specifically acting as stretchable anchors between the rigid particles thus realizing conductivity under deformation [31], [32]. In addition to electrical conductivity, such multi-filler systems can be utilized to achieve desirable thermal [33], [34] and piezoelectric [35] properties. These capabilities can enable functional material systems that can be utilized in emerging flexible electronics, soft robotics and wearable device applications where such properties under mechanical strains are critically needed.

Primary manufacturing challenge for the PC systems in general is the need for high resolution control of the filler distribution and morphology within the polymer matrix which impacts the functional properties of the final products. This challenge is more prevalent for highly complex PCs including multiple fillers such as EGaIn fillers along with rigid counterparts. Emerging additive manufacturing methods such as micro-extrusion-based printing or direct-ink-writing (DIW) carry a potential to address this challenge since it can control material deposition within layers as small as tens of microns in thickness. Studies on DIW with carbon fiber, carbon nanotube or graphene-based PCs showed that the nanofillers tend to align along the flow direction under the influence of shear and extensional stresses [36], [37], leading to increased bulk conductivity. Flow

of such inks and the associated stresses are strong functions of their shear and extensional rheology which in turn is heavily influenced by the filler type and concentration [38]. Recent studies on PC inks including liquid metal fillers demonstrated the unique properties of such material systems. Specifically, unlike rigid fillers, EGaIn fillers reduced shear and extensional viscosity of the inks while increasing their relaxation times substantially [39]. When combined with other rigid fillers, liquid metal particles and the unique rheological properties they induce can enable increased levels of control over the ink flow, resultant filler morphology and final part properties during the DIW process. To realize such capabilities, in-depth studies on the rheology of PCs including liquid metal and rigid conductive fillers, and their processing through the DIW approach is needed.

In this paper, we present an in-depth study on one of such PC systems consisting of poly(ethylene oxide) (PEO) as the polymer matrix and, EGaIn microparticles along with graphene flakes as fillers. We characterize shear and extensional rheology of the inks of various compositions derived from this system, study the flow and deposition of such inks during the DIW process along with the electrical conductivity of the printed structures. Our particular aim is to answer two key questions: (1) how the unique rheological properties inducing by EGaIn fillers in a graphene-based PC ink influence the printability and feature resolution particularly for the under-extrusion regime where the ink flow speed is less than the printing speed, (2) how do EGaIn fillers contribute to the electrical conductivity of these composites and how does this contribution vary with DIW process parameters. These studies will reveal the functional value of the liquid metal fillers when used in conjunction with other fillers, specifically regarding processability and electrical conductivity. In the following section, we introduce various ink compositions studied and their preparation, rheological characterization methods, details on the DIW experiments and characterization of the

printed structures. Results of the rheological characterization and DIW experiments are then presented along with key discussions towards answering the aforementioned questions.

2. Materials and Methods

2.1 Materials and Ink preparation

2.1.1 Materials

Composite inks studied in this work comprised of Graphene Nanopowder (Grade: AO-4: 60nm, purchased from Graphene Supermarket) and EGaIn (75% w/w Gallium from Rotometals, 25% w/w Indium from Unique Metals) microparticles as conductive fillers inside a Polyethylene Oxide (PEO) matrix. All inks were prepared in a solution form with Acetonitrile (anhydrous, 99.8%, from Sigma Aldrich) as solvent at a constant volumetric solid (filler and matrix) concentration of 30%. The overall compositions of the inks studied are summarized in Table 1. Three ink compositions that incorporate both Graphene and EGaIn fillers were used, where total filler concentration was kept at 5% by volume. The main motivation behind limiting the total filler concentration at 5% by volume, lies with our interest in the under-extrusion regime of the DIW process where the ink flow speed is less than the printing speed as detailed in Section 3.2.3. Inks with higher filler concentration than 5% exhibited both high shear viscosity and low extensional relaxation time such that continuous line formation under the specific process regime and the associated large extensional strains, was difficult.

Three distinct levels of EGaIn fillers volumetric concentration were used at 1, 2 and 2.5%. Additionally, two control inks that include the same amount of graphene fillers while replacing

	Volumetric Percentage			
	EGaIn	Graphene	PEO	Acetonitrile
EG2.5	2.5	2.5	25	70
E2G3	2	3	25	70
E1G4	1	4	25	70
G5	0	5	25	70
G2.5*	0	2.5	27.5	70
G4*	0	4	26	70

Table 1. Compositions of the inks that were studied. Control inks are marked with an asterisk.

the EGaIn volume with the PEO binder. These inks are marked with an asterisk in Table 1. The control inks were used to objectively study the influence of EGaIn fillers on the ink rheology, 3D printing behavior and electrical conductivity. A blend of two different molecular weight Polyethylene Oxide (PEO) (LWM: 105 g/mol and HMW: 5x106 g/mol, purchased from Sigma Aldrich) were used as a binder to form a polymer matrix at a weight ratio of 100:3. This approach allowed us to tune the viscoelastic behavior of the inks through relative composition of the two molecular weight polymers as described in our earlier studies [39], [40]. Inks consisting only of EGaIn fillers did not yield structures exhibiting electrical conductivity, which is expected from the earlier findings in the literature regarding the inability of EGaIn particles to form conductive pathways [29]. Given that the influence of composition and DIW-based processing on the electrical conductivity is a critical part of our analyses, we did not include any inks including only EGaIn fillers.

2.1.2 Ink Preparation

EGaIn was prepared by mixing molten gallium (75% weight) and indium (25% weight). Both metals were melted around 170^{o}C, hand mixed in a crucible for 25-35 minutes on a heated plate (Fisher Scientific, Isotemp), followed by air cooling to the room temperature. EGaIn was sonicated in Acetonitrile using a sonicator probe (YUCHENGTECH Ultrasonic Homogenizer Sonicator Processor Mixer, 600 W, 20-500ml) for about 90-120 min. The LMW PEO and Graphene nanoflakes were gradually added into the EGaIn dispersion while continuously mixing it using a mechanical mixer (Cole-Parmer Compact Digital Mixer System) at a speed of 200 RPM. The dispersion is mixed for an additional 30 minutes at a speed of 350 RPM to ensure complete dissolution of PEO and homogenization of the inks. Next, HMW PEO was steadily added to the solution. The mixing speed was reduced to 200RPM to mitigate rod climbing (or Weissenberg) [41] effects arising due to the increase in ink viscoelasticity caused by HMW PEO addition. Following the continuous mixing for another 30 min, the ink was transferred to 3cc syringes for further characterization and 3D printing experiments. The inks were stored inside sealed syringes at room temperature on a tube roller mixer to minimize settling of constituents. Pictures of a representative ink, EG2.5, stored in syringes is given in Fig. S2. The syringes were mixed in a centrifugal mixer (Thinky Mixer, Non-Vacuum, AR-100, 140g) for 40 sec before every experiment at a speed of 2000 RPM.

2.2 Rheological Characterization

Rheological characterization of the inks was performed using a rotational rheometer (TA Instruments ARES-G2) also capable of performing capillary breakup experiments for extensional rheometry. This system controls the shear and extensional strain rate precisely while measuring the torque and normal force applied between two plates between which the inks are introduced.

Through these measurement shear stress and normal stress acting the on the inks are determined to characterize their shear and extensional rheology. The specific characterization experiments are detailed below:

2.2.1 Shear Rheology

Shear rheology was characterized using cone and plate setup (50 mm diameter with a cone angle of 0.0196 rad and a gap of 0.0477 mm between the plates) and a flow ramp experiment where the strain rate was logarithmically increased from 0.1 s^{-1} to 100 s^{-1} to characterize non-Newtonian viscosity-shear rate behavior of the inks. For each ink composition one experiment using 0.64 ml ink sample was used. **During** the experiments, the ink between the plates was surrounded by mineral oil to avoid solvent evaporation. Oscillatory amplitude sweep tests were employed before running the flow ramp test to ensure that the transient material behavior is suppressed during the strain rate increase.

2.2.2 Extensional Rheology

Extensional rheometry through capillary break up experiments were performed using 0.1 ml of ink squeezed between 25 mm diameter parallel plates with an initial gap of 1 mm. The plates were moved away from each other by 12 mm at constant Hencky strain rates of 0.5,1,1.5 and 2 s^{-1} obtained through exponentially increasing velocity [42]. As such, a total of five samples of 0.1 ml ink were tested for each composition, with each sample being tested with different strain rates. The force along the motion direction was measured as a function of time while the thinning of the ink filament was observed through a microscope camera as shown in Fig 1(a). At the end of the stretching motion, the filament relaxation was further observed for an additional 20 seconds. Following the tests, mid-filament diameters were measured through image processing of the

process videos using a custom MATLAB code (Fig 1(b)). For the first part of the experiments where the top plate is in motion (stretching phase), the force vs filament diameter data was used to determine the transient extensional viscosity of the inks as a function of the Hencky strain. In the second phase where the top plate is stationary (relaxation phase), the time variation of the filament diameter is used to determine the relaxation time of various inks. While processing the relaxation data, the values extracted from the 5 tests per composition were averaged as since no clear influence of the extension rate on the material behavior during the relaxation phase was observed. This is consistent with the literature for similar materials[39], [42].

2.3 3D Printing

2.3.1 3D Printer Setup

3D printing was performed using a custom direct ink writing system as shown in Fig. 2. This system features a 3-axis motion system (Aerotech ANT180-ANT130 stages), which translates the build plate in three dimensions with sub-micron accuracy. A pneumatic time-pressure approach was used to dispense the inks during the printing process. To that end, a digital dispensing valve (Nordson UltimusPlus 1) is used to apply controlled air pressures at the back of the piston of the syringe carrying the ink with 14 kPa precision. The pressurized air source to this dispenser was regulated at 552 kPa. For experiments that require

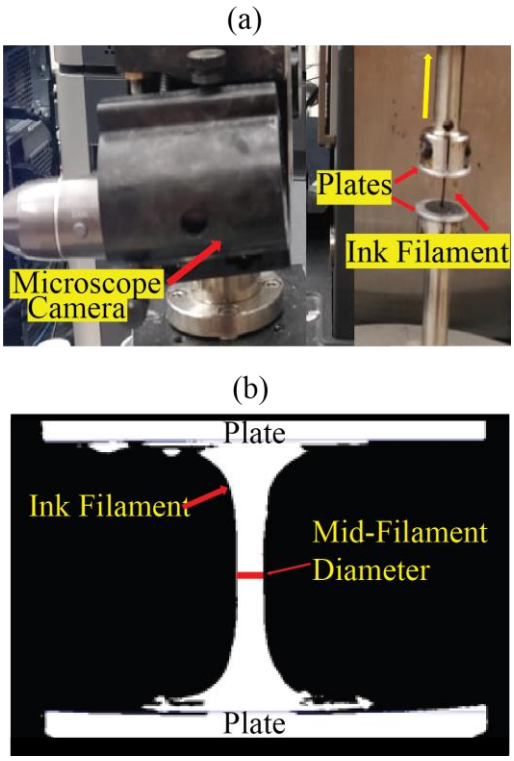

Figure 1: (a) Extensional Rheometry setup. (b) Image processing of ink filament during extensional rheology.

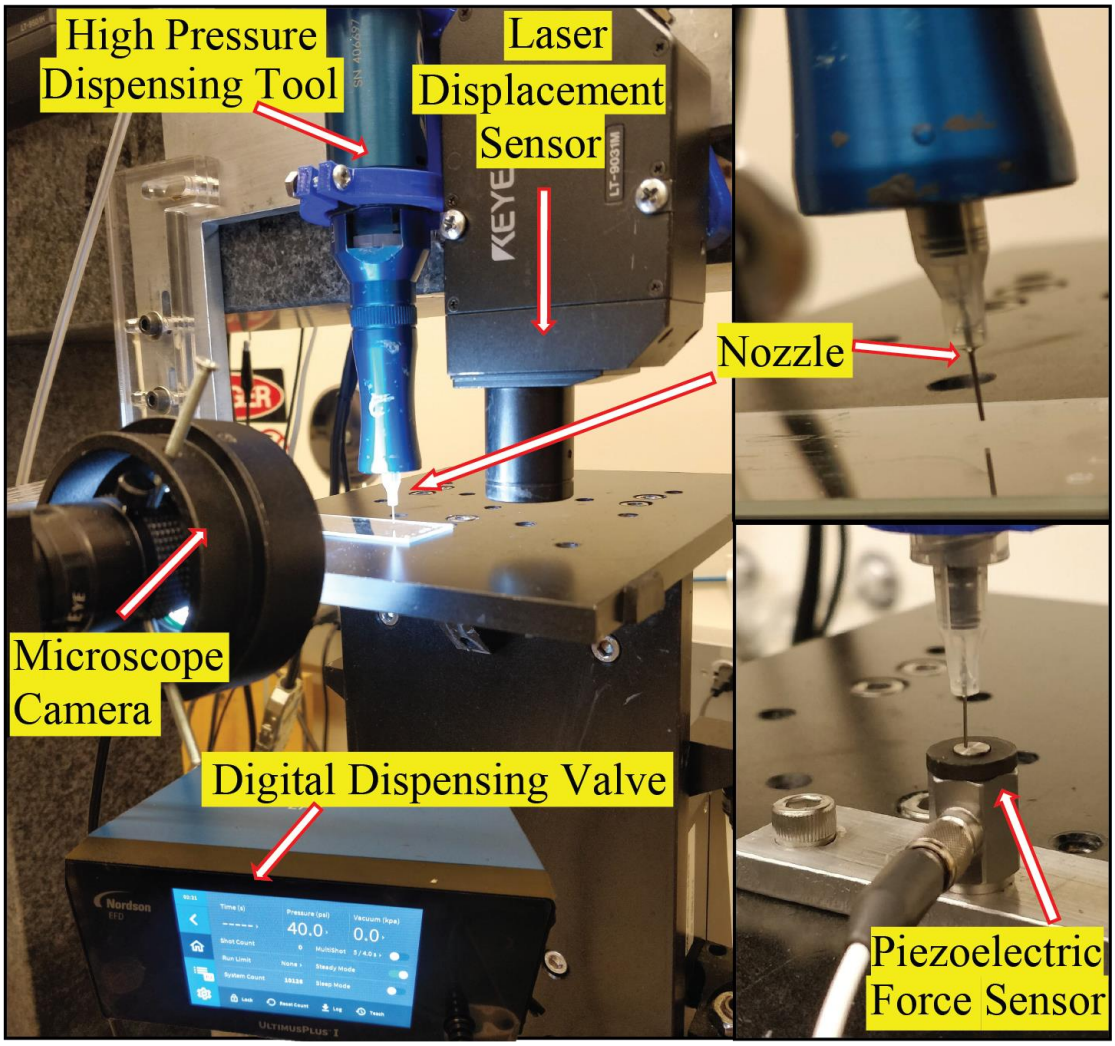

Figure 2: DIW setup.

higher dispensing pressures, high pressure dispensing tool (Nordson HP5cc) was used behind the syringe piston. To measure and precisely control nozzle-standoff distance (the distance between the nozzle and the substrate during the printing process), this system features two metrology tools: a piezoelectric force sensor (PCB Piezotronics 484B06) and a laser displacement sensor (Keyence LT9031M) (See section S1.1 in the supporting information for the detailed procedure to control the nozzle standoff distance). A custom LabView interface is used to execute the automated

printing and metrology tasks by commanding the motion stages, digital dispenser, the force sensor, and the laser displacement sensor. A microscope camera (Sentech STC MCCM200U3V) was used to visually monitor the printing process.

2.3.2 3D Printing Experiments

The 3D printing of the composite inks was explored through experiments where linear structures were printed from each ink using various sets of process parameters including flow rate, printing speed and nozzle-standoff distance. All experiments were performed using nozzles with 200 μm inner diameter (Nordson 7018462) and glass substrates. The nominal levels of flow rate, printing speed and stand-off distance that were used in the experimentation is presented in Table 2. Among these parameters the flow rates and print speeds were specifically selected to explore the under-extrusion regime of the direct-ink-writing process, where the average speed of the ink flow at the nozzle exit is less than the printing speed as demonstrated in Fig 3. Under this regime, ink filaments experience a finite "stretch" [43] after they leave the nozzle and before they are deposited onto the substrate as shown in Fig 3. The specific values of flow rates/speeds were selected through experimental observation such that a moderate dispensing pressure range between 250-950 kPa would be required to achieve these rates for the materials of interest. We observed that higher pressures lead to ink back flow near the syringe piston whereas lower pressures/flow rates are difficult to achieve in a consistent manner. Finally, the standoff distance values were

Parameters	Units			
Print Speed	mm/s	7	15	25
Standoff Distance	microns	100	200	300
Flow Rates (Average Ink Flow Speed)	m^3/s (mm/s)	3×10^{-11} (0.95)	6×10^{-11} (1.91)	9×10^{-11} (2.87)

Table 2. DIW process parameters.

selected as the 0.5, 1 and 1.5 times the nozzle diameter (200 mm). This is motivated by some of the earlier studies on the DIW process where the ratio between the standoff distance the nozzle diameter is studied [26], [43]. For each parameter set, three straight lines of 70 mm length were printed consecutively.

To achieve the desired flow rates using a time-pressure system, where the dispensing pressure, rather than the flow rate is controlled, additional experimentation was necessary. Specifically, to

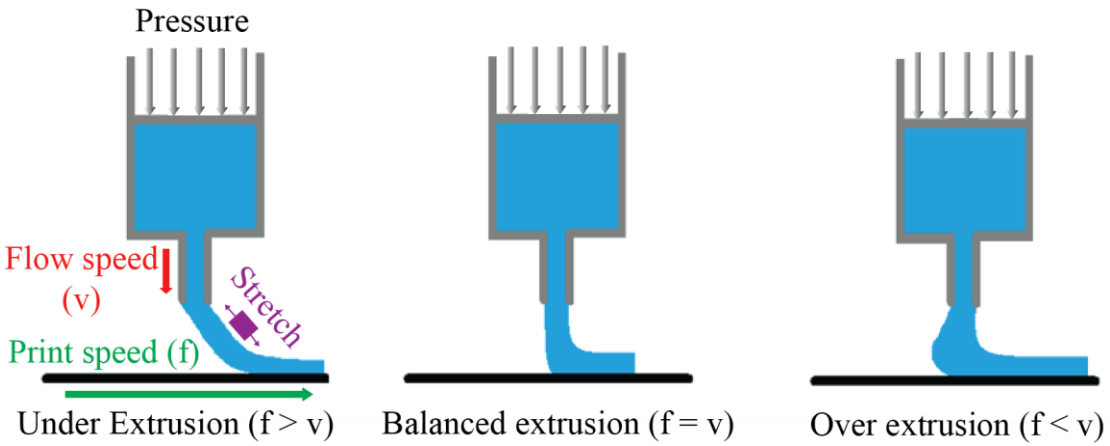

Figure 3: Various extrusion regimes in DIW.

determine the pressures required to achieve desired flow rate levels for a given material, inks were dispensed at various pressures for 120s, were collected in sealed containers and weighed. The dispensed ink volume flow rate was then calculated using known density of the inks and the dispensing duration. The three pressure levels producing the three desired flow rate levels were then used during the printing experimentation for the corresponding material. Through this approach a flow rate accuracy of 2×10-11 m3/s was achieved. The exact flow rates (with deviations around the target values within the reported accuracy) observed in the experiments were recorded and used during the analyses of the experimental data.

2.4 Characterization of the 3D printed structures

2.4.1 Geometric and Morphological Characterization

To quantitatively characterize the geometry of the prints Zygo NewView 6300 3D profilometer with a 50x scan lens was used. Geometric features such as width, height and volume were measured to calculate the electrical conductivity from resistance measurements. Scanning Electron Microscope (SEM, FEI Quanta 200F, ThermoFisher, Courtesy of WSU FMIC) with a 1000x zoom, 11mm working distance and 500V beam power was used to scan the printed lines to analyze the morphology of the composite constituents in the printed structures.

2.4.2 Electrical Conductivity Characterization

Kelvin-probe method was used to measure the DC resistance of the printed lines using an LCR meter (BK Precision Model 894, 500 kHz), to characterize their electrical conductivity. For each printing condition, the resistance of three repetition lines were measured simultaneously in a parallel fashion. Droplets of liquid EGaIn were used as conformable and low resistance electrodes [44] during these measurements to establish robust electrical contact between the measurement probes and the printed lines while avoiding damage to the lines. To this end, EGaIn droplets, large enough to cover all three lines, were dispensed at several locations along the length of the lines. Images of the lines with EGaIn contacts are included in Figure S3 of the supporting information. To eliminate the effect of contract resistance, line-transmission approach [45] was used by measuring the resistance across various lengths along the lines. Here, the resistance is represented as a linear function of the line length as follows:

$$R = \frac{1}{\sigma A} L + R_c \tag{1}$$

Where A is the average cross-sectional areas of the lines, L is the line length, determined through

optical profilometry, s is the conductivity of the lines and Rc is the total contact resistance. As such, the conductivity is calculated linear regression of the obtained R-L curves and determination of the reciprocal of their slopes and dividing them by A. The detailed experimental procedure followed to perform Kelvin-Probe and Line Transmission measurements using EGaIn contacts is explained in the Supporting Information Section S1.2.

3. Results and Discussions

3.1 Ink Rheology

3.1.1 Shear Rheology

Resulting shear viscosity and stress vs strain rate data corresponding to a representative ink, EG2.5, presented in Fig. 4(a). The data corresponding to the rest of the inks is provided in Fig S4. Generally, inks exhibited a distinct zero-shear rate viscosity and no distinct yield stress, combined with a shear thinning nature. Figure 4(b) highlights the variation of zero shear rate viscosity corresponding to different inks as obtained through fitting a Carreau-Yasuda viscosity model to this experimental data. It is evident from this data that higher graphene content leads to higher zero shear rate viscosity. EG2.5 and E1G4, compared to the control inks G2.5 and G4, did not exhibit a significantly different shear viscosity, with a slight reduction for the ink that has the higher EGaIn content, EG2.5 and a slight increase for E1G4.

3.1.2 Extensional Rheology

Resulting transient extensional viscosity vs Hencky strain data corresponding to a representative ink, EG2.5, presented in Fig 4(c). The data corresponding to the rest of the inks is provided in Fig S5. All the inks exhibited a strain hardening behavior during the stretching phase of the capillary breakup experiments, with a near constant (plateau) viscosity at low strains which increases rapidly

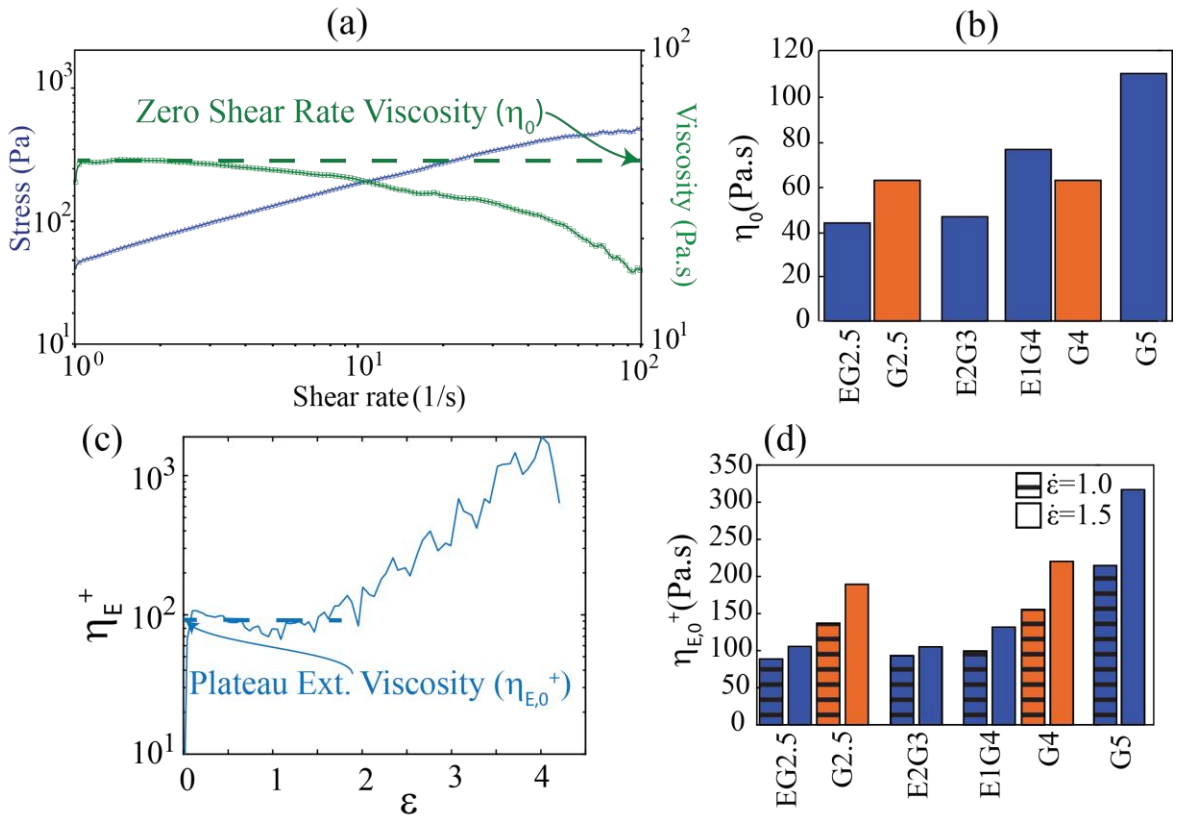

Figure 4: Results of the rheological characterization (a) Sample flow ramp test result for EG2.5, (b) Zero-shear rate viscosities of different inks, (c) Transient extensional viscosity profile of EG2.5, (d) Plateau extensional viscosities of different inks.

at high strains. Figure 4(d) shows the variation of the plateau extensional viscosity for all inks. Two data points provided for each ink represents the results obtained at two different strain rates. These results indicate that presence of the EGaIn fillers leads to a discernible decrease in extensional viscosity. Furthermore, EGaIn fillers reduce the strain-rate dependent hardening of the inks: The rate dependent increase of the extensional viscosity is higher for E1G4 compared to EG2.5, and both inks exhibit a substantially lower rate-dependent viscosity increase when compared to the control inks.

Figure 5(a) shows the relaxation profiles (normalized filament diameter vs. time during the relaxation phase of the extensional rheometry tests) for two representative inks EG2.5 and E1G4.

This data was utilized to determine the effective relaxation time for each ink through Oldroyd-B viscoelastic model fitting. Specifically, each relaxation profile was least square fitted with a three-mode Oldroyd-B model which predicts the diameter variation during relaxation as follows [46];

$$\frac{D(t)}{D(0)} = \left(\sum_{i=1}^{3} K_i \, D(0) \exp\left(-t/\lambda_i\right) \right)^{1/3} \qquad (2)$$

where K_i is a material constant that is a function of elastic modulus corresponding to a given mode and surface tension and, λ_i is the relaxation time, corresponding to a given mode, and D(t) is the filament diameter measured at time t, with t=0 corresponding to the instant where the top plate stops moving during the experiments. The representative model fits are shown in Fig 5(a). The data corresponding to the rest of the inks is provided in Fig S6. Following this fitting, the highest relaxation time across the three modes were selected as the effective relaxation time for the material [46]. The average relaxation times were accordingly calculated for each material across different experiments and shown in Fig 5(b). It is evident from this figure that inclusion of EGaIn fillers yield a distinct increase in relaxation time of the inks. This result is consistent with the earlier findings regarding the PEO-EGaIn composites (without graphene) [39] and can be explained by the elasticity of the oxide covered liquid EGaIn particles [47].

3.2 3D Printing

Results of the experiments outlined in 2.3.2 were categorized to four categories as function of the general morphology of the printed lines as illustrated in Fig 6(a). Here, continuous (C) prints refer to lines that were generated with homogenous width throughout their lengths, marginally continuous (MC) lines, despite being connected throughout. show local reductions in width at several locations, “blobby” (B) lines show a periodic pattern consisting of a large ink deposit

followed by a thin line, discontinuous (D) lines exhibit disconnections of various lengths. Videos of the printing processes leading to each of the four types of lines is provi ded as a part of the supporting information. During the printing of C-type lines, the ink forms a steady filament that is stretched under extensional flow (since the under-extrusion regime is studied) between the nozzle and the substrate as it is being deposited. B-type lines are observed when the ink flowing out of the nozzle forms a growing bubble at the nozzle exit rather than exhibiting extensional flow between the nozzle and the substrate as observed in the C-type lines. When the height of the bubble reaches the standoff distance, it is deposited on the substrate, forming a transient filament between the nozzle and the substrate, which thins down as a new droplet forms but does not fail until the new droplet gets deposited. MC-types lines exhibit rather sporadic transitions between the C and B type lines, likely due to small variations in the ink composition that is flowing through the nozzles. In the case of the D-type lines, the filaments forming between the nozzle and the substrate fail leading to a disconnected pattern. To understand how the ink rheology and the printing parameters influence the formation of these different results, we considered two non-dimensional parameters:

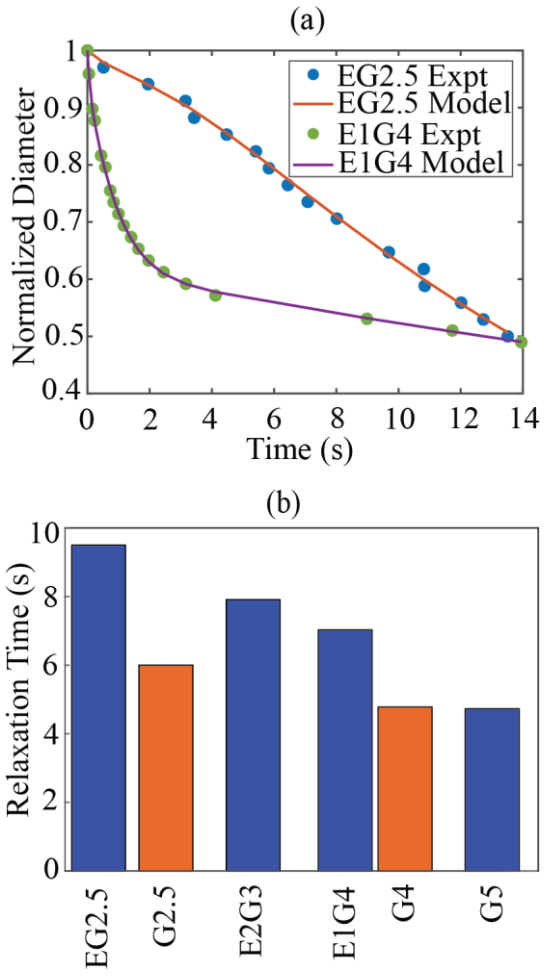

Figure 5: Characterization of the relaxation behavior of various inks; (a) Temporal relaxation profile of two sample inks along with the 3-mode Oldroyd-B model fits, (b) Relaxation times of different inks.

$\epsilon = 4Q/\pi D^2 f$ and $Ec = \sigma\lambda/\eta_0 H$. Here, the printing strain (ϵ) is the strain experienced by the printed filament as it flows between the nozzle and the substrate. It is simply the ratio between the average speed of the ink exiting the nozzle and the printing speed (i.e. the speed of the substrate), incorporating the ink flow rate Q, nozzle diameter D and printing speed f. The Elastocapillary number (Ec) is a commonly used non-dimensional parameter that quantifies the interplay between the capillary-elastic and viscous effects in a given material-process pair [48], [49]. Here s is the surface tension, l is the relaxation time and h0 is the zero-shear rate viscosity of the inks and H is the stand-off distance during printing. All these parameters other than surface tension is either characterized through the results presented in Section 3.1 or prescribed during the experiments, except for the surface tension. For viscoelastic materials such as the inks considered in this work, the free surface behavior is heavily dominated by elastic and viscous effects rather than surface tension [50] which renders the use of conventional experimental techniques to measure surface tension, such as pendant drop, impossible. In the limited number of studies in the literature which focus on polymer solutions or composite inks with low solid concentration, it has been shown that variation in polymer and particle concentration causes a deviation from the solvent surface tension generally within 1-1.5% per 1% increase in solid concentration [51], [52]. Since the main purpose of this analysis is to compare the Ec values across the inks of interest, we consider the fact that the solute concentration for all the inks is the same at 30% and the particle composition varies only within 2.5% volumetrically. We accordingly implemented constant surface tension value across the inks, equal to the surface tension of solvent Acetonitrile (0.02929 N/m).

The portion of the Elastocapillary number that represents material rheology is given by $Ec^* = HEc$, which we refer to as the Elastocapillary height of a given ink. This quantity was calculated

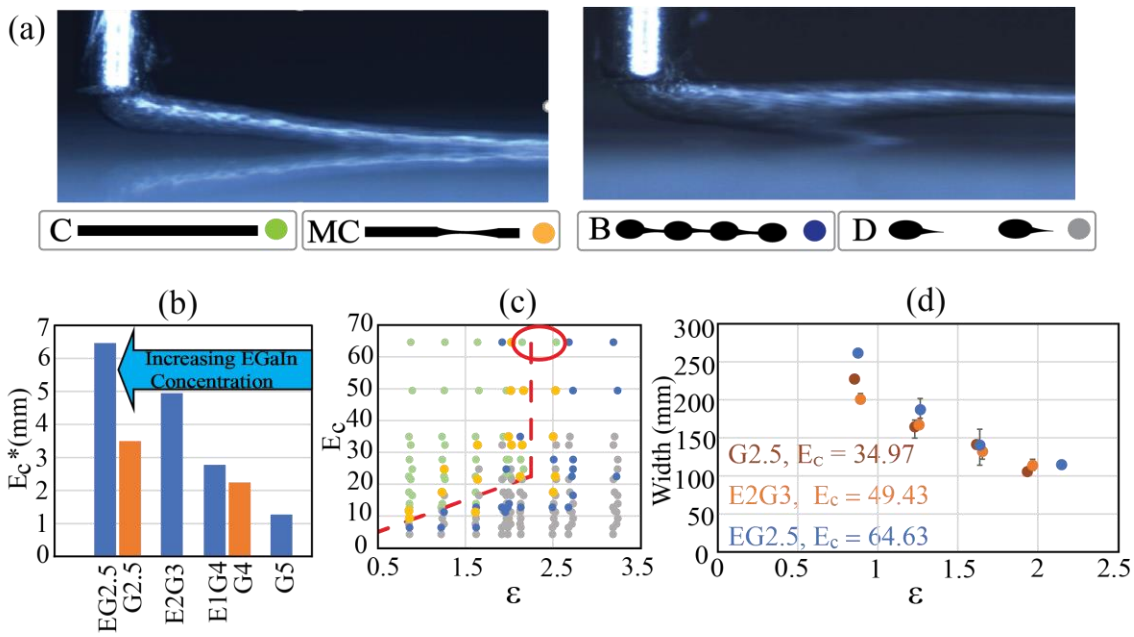

Figure 6: Results of the printing experiments; (a) Morphological categorization of the printed lines, (b) Ec* values for each ink, (c) Results of all printing experiments on the Ec-ε plane. Each experiment is represented with a dot, the color of which is determined by the categorization given above, (d) Strain dependent variation of linewidth for three materials.

for each ink using the relaxation time and zero-shear rate characteristics detailed in Section 3.1. Figure 6(b) illustrates that the Ec^* increases with the increasing EGaIn and decreasing Graphene content in the inks, due to the increased relaxation time and reduced shear viscosity. Comparison of the Ec^* values between the EG2.5 and G2.5 as well E1G4 and G4 inks demonstrate the distinct influence of EGaIn fillers on the elastocapillarity of the inks.

Figure 6(c) presents the classification of all printed lines mapped in the ϵ-Ec plane. Here, each experiment is denoted with a single circle, color of which depicts the classification of the result. Several key conclusions can be drawn from this map. Intuitively, continuous lines are formed at lower strains (i.e. lower printing speeds and higher flow rates). Interestingly, the strain level below which the continuous lines can be obtained varies with the Ec value such that this limiting strain

is between 2-2.5 for Ec values higher than ~20 with a few notable exceptions at the highest Ec levels. At lower Ec values, the limiting strain reduces almost linearly with reducing Ec value. The red dashed lines were added to highlight the apparent region in the ϵ-Ec plane within which continuous prints were obtained.

As mentioned above, inclusion of EGaIn fillers increases the Ec^* of the inks, leading to a higher Ec value for constant standoff height during printing. To capture that effect and its influence of the line continuity, Fig. S5 in the supporting information separates the same results into plots corresponding to each material. These plots demonstrate that the general continuity of the lines increases with the increasing EGaIn content in the inks. It can be concluded that the increased Ec^* (through increased relaxation time and reduced viscosity) induced by the high EGaIn particle and/or low graphene content enables printability at lower flow rates and higher printing speeds (i.e. higher strains) and higher stand-off distances. In the rheological context, the elastocapillary number represents the relative strength of the elastic effects with respect to the viscous effects in a given liquid [48]. Considering the results regarding elastocapillary lengths of different ink compositions, one could conclude that EGaIn fillers thus "strengthen" the elastic effects which promotes a deposition mechanism where a stable ink filament is stretched between the nozzle and the substrate, whereas the graphene fillers generally induce an inverse effect. This result is consistent with our earlier findings involving EGaIn and Graphene only composite inks [39]. As these elastic effects weaken, viscous effects promote a mechanism where the ink that exits the nozzle form droplets rather than continuous filaments in tension leading to B-type line formation, particularly observed at high standoff distances. The distinct influence of the EGaIn fillers towards printability at high strains can be observed through the two specific data points circled in Figure

6(c) indicating continuous prints at strain levels over 2. These two data points belong to the EG2.5 formulation and under the same conditions the control ink G2.5 failed to achieve continuous prints.

Printed filaments forming continuous lines at strains higher than 1 (i.e. under-extrusion condition) are expected to undergo visco-capillary thinning which reduces the lateral line width. Figure 6(d) presents the width of the lines, measured through optical profilometry. The linewidths measured around the strain of 1 (i.e. balanced extrusion) can be observed to be larger than the nozzle diameter of 200 μm. This result can be explained by the spreading of the inks after their deposition on the glass substrates. It should be noted that these width measurements were taken after spreading of the ink on the glass substrates and drying of the ink solvent. Considering that the solvent constitutes 70% of the ink volume, considerable spreading of the inks following the deposition is expected.

At low strain levels, the linewidths at the highest Ec value, corresponding to the ink EG2.5 are larger compared to the two other cases. High amount of spreading of EG2.5 can be linked to its low shear viscosity and high density (due to the high density of EGaIn), given that the gravitational effects are a critical contributor in ink spreading [53]. This postulation is somewhat contradicted by the fact that the spreading of G2.5 (Ec=34.97) is higher than E2G3 (Ec=49.44) despite its higher viscosity and lower density. This discrepancy can possibly be explained by (1) slightly lower value of the exact strain recorded for G2.5, indicating that the actual measured flow rate is slightly higher compared to the other two cases and (2) possible contact line pinning effects induced by the higher graphene concentration suppressing the spreading behavior [54]. Nevertheless, at higher strains, line widths of these three materials are closer to one another as the capillary effects due to solvent's surface tension starts to dominate the inertial flow effects. Among these cases, only EG2.5 with the highest Ec value can "survive" strains over 2 for which the linewidths as small as 100 μm can

be obtained. These results reveal that increased ink elasticity induced by the EGaIn fillers in these composites enable lateral printing resolution that is smaller than the nozzle diameters.

3.3 Electrical Conductivity

The electrical conductivities of the lines printed using different inks at the lowest tested strain and stand-off distance levels are presented in Figure 7(a). Under these conditions, the inks are deposited near the balanced extrusion regime thus the measured conductivity values are isolated from the effects coming from ink filament deformation outside the nozzle. From this plot, it could be inferred that graphene fillers are the main contributors to the conductivity. To understand the influence of EGaIn on the composite conductivity, one can compare the conductivity of EG2.5 and E1G4 with their corresponding control inks G2.5 and G4, respectively. As such, EG2.5 exhibit significantly higher electrical conductivity than G2.5 whereas E1G4 and G4 inks exhibit nearly the same conductivity.

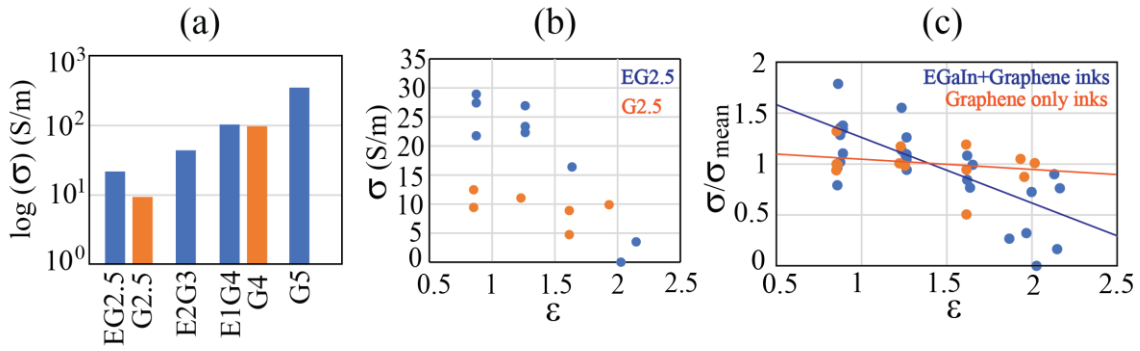

Figure 7: Results of the electrical conductivity characterization; (a) Conductivity of each tested material, obtained near balanced extrusion with the lowest standoff distance, (b) Strain-dependent variation of electrical conductivity of EG2.5 and G2.5, (c) Strain-dependent variation of normalized electrical conductivity for composites with EGaIn-Graphene and only Graphene fillers.

These results indicate that EGaIn fillers increase the electrical conductivity of the composite, particularly at high EGaIn filler concentrations. Further analysis involving a large set and variety

of inks is necessary to robustly assess and quantify this contribution. It should be noted that this is not a trivial finding. As indicated by several studies cited in the introduction, the oxide skin encapsulating such particles are known to prevent them forming conductive connections. Accordingly, it can be preliminarily concluded that the contribution of the EGaIn fillers to conductivity is a function of the other conductive fillers in the composite.

To understand how this contribution vary with strain, Fig 7(b) compares the variation of electrical conductivity of EG2.5 and G2.5 lines as a function of printing strain. As shown, the conductivity of EG2.5 lines reduce with increasing strain values, unlike G2.5 in a similar strain range. To see if this behavior holds throughout out the tested ink compositions, we calculated normalized conductivity values for each printed line by dividing the line conductivity with the average conductivity of all the continuous lines from the same material and plotted the results as a function of strain in Fig 7 (c), separately for inks that include and exclude EGaIn fillers. This normalization enables comparison of inks with varying graphene content by removing the inherent material conductivity differences. As indicated by the linear regression lines, presence of EGaIn fillers generally induce a strain dependent conductivity behavior in the printed structures.

To understand the mechanism behind this behavior, we examined the scanning electron microscope images of the printed lines, focusing on the EG2.5 inks. We observed the morphology of the ink constituents on the surface of the printed lines. We focused on two regions: center of the lines where target printing speed and, thus strain is in effect (Fig 8(a)) and at the end points where the printing speed is down to zero, thus no strain is present (Fig 8(b)). As shown, EGaIn fillers that are normally circular under zero strain, tend to take elliptical shapes under positive strains, with their major axes aligned along the printing direction. To analyze this quantitatively, we used image

processing (ImageJ software) to measure particle dimensions parallel (W) and perpendicular (H) to the printing direction for several experiments as illustrated in Fig 8(c). To this end, we considered three experiments with varying strain levels, calculated the average H/W ratio corresponding to 15 particles extracted from both the center and end points of the printed lines, and plotted the difference between these ratios corresponding to the center and end points and presented in Fig 8(d). Here, smaller H/W ratio indicates a larger particle deformation from circular shape (for which H/W=1). The line end points where no strain is present, is used a reference for each experiment through the ratio difference calculation. As shown, the ratio difference increases with increasing strain, indicating increasing stretching of the EGaIn particles along the printing direction. The individual H/W ratios for the end and center points of the lines studied in this analysis is provided in the supporting information, Fig. S8.

This deformation is expected due to the liquid phase cores of these filler particles at this particular size scale [47]. Furthermore, such a deformation will increase the electrical resistance of an isolated particle. Given that the EGaIn fillers contribute to the bulk conductivity, it can be postulated that the conduction through these fillers is a part of the electrical conduction mechanism of these composites. Accordingly, increase in the resistance of the particles yields a reduction in the bulk conductivity of the composite as observed in Fig 7(c). It should be noted that a secondary mechanism through which increasing printing strain reduces electrical conductivity would be the stretching of the binder phase and the associated separation of the conductive graphene flakes. In fact, presence of such an effect is evident from the slight strain-dependent reduction of the conductivity of the non-EGaIn containing inks in Fig 7(c). However, substantially higher rate at which the conductivity of EGaIn containing inks reduce with printing strain indicates that the filler

p article deformation is likely the dominant mechanism of conductivity variation in these inks.

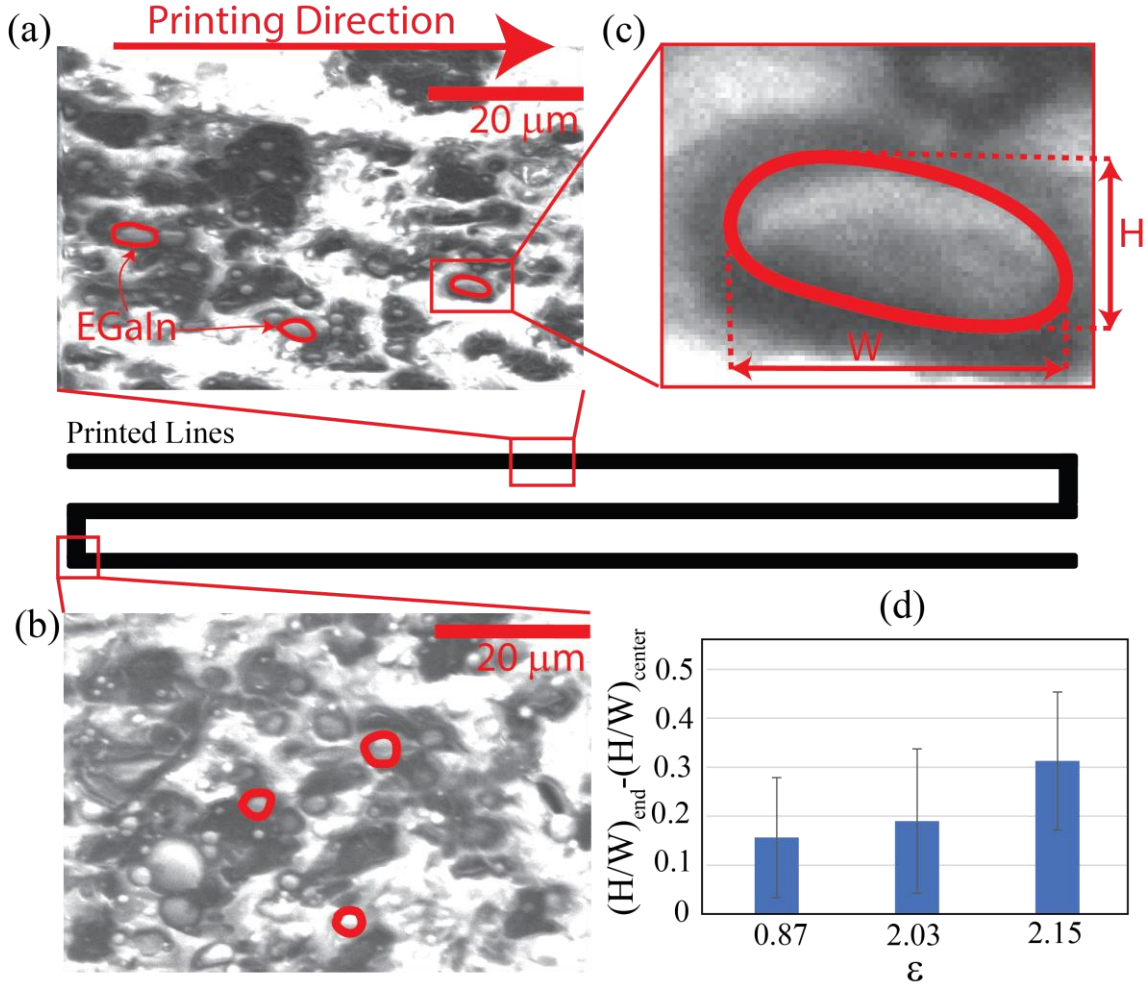

Figure 8: SEM characterization of the EG2.5 lines; (a) SEM image obtained from the line center, (b) SEM image obtained from the line end, (c) Details of the width and height measurement of the EGaIn particles, (d) H/W ratio difference as a function of printing strain.

4. Conclusions and Outlook

Presented results demonstrate that liquid metal fillers introduce viscoelasticity to graphene-PEO composites inks, which substantially improve the processability of this material system, specifically through direct-ink-writing. Particularly, inks including EGaIn fillers could be printed at combinations of higher speeds, lower flow rates and higher standoff distances, allowing more

robust, higher throughput application of additive manufacturing in processing of PCs. The capability of EGaIn including inks to withstand high extensional strains and associated viscoelastic thinning enables printing of filaments that are substantially smaller than nozzle diameter, increasing the process resolution. Regarding electrical properties, we have obtained preliminary evidence that EGaIn fillers also increase the inherent conductivity of the graphene-PEO composites. More importantly, the electrical conductivity of the EGaIn including composites is a strong function of printing process parameters, enabling spatial control of the conductivity in 3D printed composites through variation of process parameters such as speed and flow rate. These findings indicate that PCs including EGaIn fillers carry a great potential to advance the applications utilizing conductive PCs, particularly emerging technologies that are powered by the unique capabilities of additive manufacturing and can benefit from precise control of electrical conductivity. These applications include flexible-stretchable electronics [16], biochemical sensors [17] and printable energy devices [55].

Future research outlook includes several key directions: One of these directions is a detailed study of the influence of EGaIn fillers on the mechanical properties of the complex 3D printed structures of graphene composites. Secondly, inks with higher graphene content should be investigated. Such inks are known to exhibit high viscosities and yield stresses dominated by particle networks of graphene, rendering them difficult to process through direct-ink-writing [38]. EGaIn fillers and the associated viscoelasticity induced in the ink rheology can potentially increase the processability of such inks by reducing shear viscosity and yield stress, allowing shear and extensional flow induced alignment of graphene fillers at higher graphene concentrations, that would normally be hindered by plug flow effects [56], realizing composites with unprecedent levels of electrical conductivity.

Finally, combination of EGaIn fillers with other carbonous (e.g. graphite, carbon nanotubes etc.) or metallic (i.e. silver, gold nanoparticles) fillers as well as different polymer binders should be explored.

CHAPTER THREE: FLOW MECHANISMS AND THEIR INFLUENCE ON THE PROPERTIES OF EGAIN-GRAPHENE-POLY(ETHYLENE OXIDE) COMPOSITES DURING MATERIAL EXTRUSION-BASED ADDITIVE MANUFACTURING

1. Introduction

Polymer composites (PC) exhibit unique bulk properties by synergistically combining the properties of fillers particles (thermal and electrical conductivity) and polymer matrices (high modulus, toughness, elasticity). Due to these exceptional material properties, PCs are eminently used for applications such as soft robotics, energy storage devices, flexible electronics and tissue engineering. The functionality of parts and devices used for these applications is a strong function of the microstructure of the composites which is governed by their processing. Among the processing methods used for PCs, material extrusion-based additive manufacturing methods, particularly direct-ink-writing (DIW), has recently emerged as a favorable technique, due to its capability to direct filler morphology within each deposited micro-filament [57] . Processing-property relationships for DIW are governed by the complex ink flow mechanisms which are manifestations of ink rheology and ink-nozzle interactions such as wall-slip. As such, there is a need for fundamental research to understand these relationships towards realizing precise control over the properties of printed polymer composite structures.

Direct-Ink-Writing has been commonly applied to PCs featuring conductive solid-state micro and nano-fillers including carbonous ones such as carbon fibers[58], [59], graphene flakes[60], graphite particles[61], and carbon nanotubes[62] metallic ones such Ag, Cu [63], [64]. Recently, particles of Gallium-based liquid metal (LM) alloys like Ga-In (commonly referred to eutectic GaIn or EGaIn), Ga-Tin have been considered as fillers in PCs. These spherical particles of diameters ranging from tens of nm to hundreds of microns can be created by ultrasonication of bulk liquid metals in various liquid media including solvents [65], [66] and polymer solutions[67]. They exhibit a unique morphology at room temperature as they consist of a liquid core and solid shell of Ga2O3 for particles that are larger than 70 nanometer in diameter [68]. This unique nature renders these particles deformable unlike any other conductive fillers. This property has recently been shown to significantly influence the processing of the LM particle-based PCs, particularly

DIW type additive manufacturing. [69]. LM particles have also been used as secondary fillers in PCs, accompanying rigid fillers such as graphene[70] , Ag [71], etc. In such systems, LM fillers can act as stretchable anchors ensuring conductivity under large strains [72] or improve the thermal [70], [73] piezoelectric properties[74] of the composites. Our earlier work has shown that LM fillers significantly affected the rheology and processing of the complex precursors of such material systems[60], [75]. Particularly in the case of direct-ink-writing using solvent-based inks including graphene as a rigid filler, it was shown that the introduction of EGaIn particles increases the ink viscoelasticity and improves the printability through DIW [60]. These results highlight the need for further studies on the composition-processing-property relationships pertaining to DIW of LM-based PCs, particularly how LMs can influence the microstructural evolution of PCs during DIW.

It is known that shear and extensional flows experienced by the composite inks inside the printing nozzles drive the morphology of the fillers, directly dictating the final microstructure and functional properties. Ink rheology is a critical factor determining the nature of such flows, yet, understanding ink rheology is not sufficient to fully understand shear and extensional flows in a quantitative sense. The other critical and often overlooked factor influencing ink flow is wall-slip, which is particularly prominent for PC inks with high solid loading [76], [77]. Increasing wall slip generally reduces the magnitude of shear strain rates that are responsible for filler alignment [58] , hindering the capability of DIW to dictate the part microstructure. Despite this conventional understanding, in-depth study on how wall-slip affects the part microstructure evolution during DIW of PCs is missing. Furthermore, the influence of LM particles included in PC inks on the wall slip during DIW is not clear, particularly given their deformable nature unlike solid fillers.

In this paper, we aim to address some of these gaps in the literature through an in-depth study of the compositional and process related factors that determine the electrical conductivity of the printed PCs consisting of EGaIn particles and graphene flakes in a Polyethylene Oxide binder. Particularly, the effect of ink composition, nozzle size and flow rate on printed parts electrical conductivity is investigated. In that, a mechanistic understanding is sought after through studying how these variables dictate key aspects of ink flow such as wall slip and shear deformation rate which are known to influence part microstructure and thus conductivity. This analysis has been

performed through extensive capillary and rotational rheometry of various ink compositions. The rheological characterization data has been used to model of non-Newtonian capillary flow of inks through the nozzles incorporating non-linear wall slip effects. Finally, test structures were printed and their electrical conductivity were characterized.

2. Materials and Methods

2.1 Materials and Ink Preparation

Inks used in this study consist of a Polyethylene Oxide (PEO) blend as a binder, two types of conductive fillers; Graphene nano-powder (Grade: AO-. 4: 60nm, purchased from Graphene Supermarket) and EGaIn micro particles (75% Gallium, 25% Indium by weight), in an Acetonitrile medium (anhydrous, 99.8%). The PEO blend consists of two different molecular weight PEO (LWM: 105 g/mol and HMW: 5x106 g/mol, purchased from Sigma Aldrich). Various ink compositions studied in this work are listed in Table 1.

Ink preparation starts with bulk EGaIn being broken into smaller segments in acet

TERMS	EGaIn	Graphene	PEO	ACETONITRILE
E1.8G12.1P13.9	1.8	12.1	13.9	72
E2.9G11.6P14.4	2.9	11.6	14.4	71.1
E3.8G10.4P14.2	3.8	10.4	14.2	71.7
E5G10P15	5	10	15	70
E2.6G10.5P17.1	2.6	10.5	17.1	69.82
E0.5G10.8P17	0.5	10.8	17	71.7
E1.93G9.67P17.41	1.93	9.67	17.41	70.99
E2.9G8.7P17.5	2.9	8.7	17.5	70.9
E2G11.2P15.3	2	11.2	15.3	71.5
E0G12P15	0	12	15	74
E0G10.2P13.9	0	10.2	13.9	75.9

Table 1. Volumetric compositions and the names of the inks used. Values are given in % vol

onitrile using a vortex mixer (Oxford BenchMate Mini Vortex Mixer) followed by ultrasonication (YUCHENGTECH Ultrasonic Homogenizer Sonicator Processor Mixer, 600 W, 20-500ml) to form particles. Particles have an average size of 2.5 mm with a standard deviation of 1.2 mm evalu

ated among 500 particles imaged through SEM. The particle size distribution is given in supporting information Fig S1. LMW PEO and graphene were gradually added using a mechanical mixer (Cole-Parmer Compact Digital Mixer System) at the speed of 300 RPM. After 25mins of continuous mixing, HMW PEO was gradually added at 150-200 RPM to avoid the rod climbing effect. This ink was continuously mixed for an additional 15 -20 mins to obtain a homogenous paste and then was stored in 30cc syringes. Prior to experimentation, the inks were transferred to a 5cc steel syringe which was centrifuged at 4000 RPM (using a Nordson Processmate 5000 centrifuge) for 30-60 to evacuate the trapped air.

2.2 Characterization and Modeling of Shear Flow and Wall Slip

2.2.1 Shear Rheology:

The shear rheology of these inks was characterized using the TA instrument Ares G2 strain-controlled rotational rheometer. To this end, a flow sweep experiment was performed for each ink composition. A serrated parallel plate geometry with a diameter of 25mm was used to conduct the experiments. A plate gap of 1 mm was utilized, and non-volatile mineral oil was applied at the outer rim plates to prevent solvent evaporation from the inks during the experiments. Prior to the experiments, the material samples were pre-sheared at a strain rate of 1e-3 s-1 to overcome the transient effects. The flow sweeps were performed at strain rate range from 5x10-4 s-1 to 5x10-2 s-1 to determine the rate dependent shear stress profile for each material. The flow sweep tests were run in the decreasing strain rate direction to reduce the transient effects that are commonly observed at low strain rates.

2.2.2 Capillary Rheometry

Capillary rheometry tests were performed for each ink composition using a custom-built hybrid DIW printhead with capillary rheometry capability. A brief description of this system is provided in the supporting information section S1 and it is described in detail in our earlier work [78]. This system gives us the capability to prescribe an extrusion pressure and monitor the steady-state flow rate in real time.

In capillary rheometry experiments, nozzles having four different diameters (250, 300, 400 and 600 mm) with two different lengths (13mm and 25.4mm) were used. These tests were conducted

by extruding each material at four different flow rates for each nozzle corresponding to the apparent strain rates that are in the 9 to 125 s-1 range. Here, the apparent strain rate ($\dot{\gamma}_a$) is given by

$$\dot{\gamma}_a = \frac{4 \times Q}{\pi \times R^3} \quad (1)$$

where Q is the ink flow rate and r is the radius of the nozzle. To produce the flow rate vs. pressure data for each material-nozzle combination, first, the extrusion pressure yielding a flow rate corresponding to the low end of the strain rate range is determined. Next, three additional pressures were iteratively selected to ensure that approximately the same flow rates are tested for nozzles having the same diameter but different lengths, while staying within the system's allowable pressure range of 5-225psi. As a result, the exact values of the apparent strain rate were marginally different for each ink composition. These exact values are provided in the supporting information Table S1.

The pressure vs. flow rate (P-Q) data obtained for each nozzle-ink composition were then fitted a power-law function in the general form

$$P_{R,L} = K_{R,L} Q^{n_{R,L}} \quad (2)$$

where KR,L and nR,L are power-law parameters corresponding to the nozzle with radius R and length L. These equations were then utilized to perform the Bagley analysis to determine the true wall shear stress for each experiment. To this end, for a given ink, we determine the maximum and minimum flowrate measured for each nozzle radius across the two lengths. Six equidistant flowrate points were then calculated in this range. For each flowrate point, the apparent strain rate was calculated using Eq. 1. The corresponding pressures were calculated for two different lengths of the nozzle radius using Eq. 2. The actual wall shear stress for all the flow flowrate points were then calculated by linear regression between the pressures calculated for each nozzle length with respect to the length over radius ratio as follows.

$$P_{R,L} = 2\,\tau_{w,R}\left(\frac{L}{R}\right) + P_{ent,R} \quad (3)$$

where $\tau_{w,R}$ is the actual wall shear stress and $P_{ent,R}$ is the pressure loss at the nozzle entrance. [79] Next, the apparent strain rate vs. true wall stress data across the determined flow rates were fitted with a power law as

$$\dot{\gamma}_{a,R} = A_R {\tau_{w,R}}^{m_R} \quad (4)$$

Pressure loss at the entry is equal to the extensional stress the ink experiences as it enters the narrow nozzle capillary[79].

2.2.3 Model Fitting

To elucidate the flow mechanisms, specifically the contribution of wall slip and shear to the overall ink flow for different ink compositions under various DIW process conditions, we utilize the rotational and capillary rheometry data to construct a process model. This model correlates the apparent strain rate observed during the ink flow to its two main contributors that are wall slip and shear flow[76], [80]

$$\dot{\gamma}_a = \dot{\gamma}_a^{slip} + \dot{\gamma}_a^{shear} \quad (5)$$

Each of these terms are explicitly correlated to the shear stress at the wall and several material properties. Particularly, the slip portion is given by

$$\dot{\gamma}_a^{slip} = \frac{4\beta\tau^m}{R^{x+1}} \quad (6)$$

Where t is the wall shear stress, b, m and x are constants representing the non-linear relationship between the wall slip and the shear stress [80]. The shear term is given by the general formula [76]:

$$\dot{\gamma}_a^{shear} = \frac{4}{\tau^3}\int_0^{\tau} \tau^4 \dot{\gamma}(\tau) d\tau \quad (7)$$

Where $\dot{\gamma}$ is the true rate of shear experienced by the ink. For this term to evaluate, the functional relationship between the shear stress and the strain rate of the material needs to be known. For most highly loaded inks, the Herschel-Bulkley material model is a good representation of this functional relationship [81]:

$$\dot{\gamma}(\tau) = \frac{\left(\tau - \tau_y\right)^{1/n}}{K} \quad (8)$$

Where τ_y is the yield stress, K is the consistency and the n is the power-law index of the material. With this model integrated, the shear component of the apparent strain rate becomes,

$$\dot{\gamma}_a^{shear} = \frac{4\tau^{1/n}}{K^{1/n}}\left(\frac{\tau_y^2(1-\tau_y/\tau)^{1+1/n})}{\tau^2(1+1/n)} + \frac{2\tau_y(1-\tau_y/\tau)^{2+1/n})}{\tau(2+1/n)} + \frac{(1-\tau_y/\tau)^{3+1/n})}{(3+1/n)}\right) \quad 9$$

To perform the model fitting, capillary rheometry data is fitted to Eqs. 5, 6 and 9, while simultaneously the rotational rheometry data is fitted to Eq. 8, by optimizing the constants, b, m ,x, K, n and τ_y. The capillary rheometry data for this fitting practice is populated using Eq. 4 for each composition- nozzle pair, within the tested wall stress range. The model fitting was performed as a bounded non-linear optimization using fmincon function of MATLAB which uses the interior-point algorithm[82]. Here each variable is bounded to be greater than 0 to ensure physicality and the n variable was bounded between 0 and 1 to ensure shear thinning nature. The starting guesses for each variable were varied to ensure no significant variation in the final result is observed due to local minima complications.

This model is then used for each printing experiment to determine several key parameters elucidating the ink flow mechanisms pertaining to wall slip and shear. Particularly, the true shear strain rate the ink experiences at the nozzle wall is given by

$$\dot{\gamma}(R) = \frac{\tau^{1/n}}{K^{1/n}}(1-\tau_y/\tau)^{1/n} \quad 10$$

Here, to determine the wall shear stress (τ) can be calculated by first estimating the pressure required to achieve the same flow rate as the printing experiments but with a longer nozzle, using the Eq. 2. This equation is then used along with the flow rate and pressure measured during the printing with a shorter nozzle to apply the Bagley correction and determine the true wall stress and entrance pressure loss (P_{ent}) using Eq. 3.

Here, the slip velocity is given by

$$v_s = \frac{\beta\tau^m}{R^x} \quad 11$$

The percent contribution of wall slip and shear mechanisms to the total apparent strain rate are then given by:

$$PC_{slip} = \frac{\dot{\gamma}_a^{slip}}{\dot{\gamma}_a} \times 100\ , PC_{shear} = \frac{\dot{\gamma}_a^{shear}}{\dot{\gamma}_a} \times 100 \quad 12$$

Finally, the pressure loss at the nozzle entry was used to estimate the rate of extensional strain ink experiences using the Cogswell method[83] as follows:

$$\dot{\varepsilon} = \frac{4\tau\dot{\gamma}_a}{3(1+1/m_R)P_{ent}} \quad (13)$$

2.3 Direct-Ink-Writing (DIW) Experiments and Print Characterization

2.3.1 DIW Experiment Parameters

DIW experiments were conducted to study how different flow mechanisms influence the properties of the 3D printed composites. To this end, the custom-built hybrid DIW printhead was used to print lines at various flow rate levels for each ink composition. Steel nozzles with four different diameters of 250, 300, 400 and 600 mm were used with a constant length of 13 mm. Lines were printed on glass substrates with a standoff distance equal to the nozzle diameter. For each ink composition, three apparent strain rate levels were determined and kept constant across nozzle sizes. These strain rates were calculated through Eq. 1 using the lowest, highest and the midpoint flowrates from the capillary rheometry experiments corresponding to the 600 mm diameter nozzle. The corresponding flowrates for the other three nozzles were then calculated at these apparent strain rate levels using Eq. 1. Printing was performed using the constant pressure mode of the printhead that allows for rapid stabilization of the flow rate. [78] The P-Q relation data obtained in Sec. 2.1.3. was used to determine pressure levels required to print the ink at the predetermined flowrates for each nozzle.

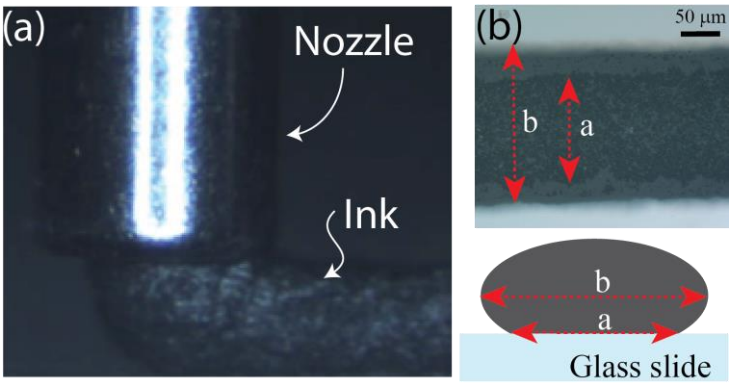

Figure 1. (a) Microscope image of the DIW process, (b) Details of the cross-sectional area analysis

The substrate was hosted on a 3-axis motion system (Aerotech ANT180-ANT130 stages) to generate the printing motions whereas the printhead was kept stationary. The printing speeds were selected to be equal to the average speed of the ink flow at the nozzle exit to ensure balanced extrusion:

$$f = \frac{Q}{\pi R^2} \quad (14)$$

where f is the printing speed, Q is the ink flow rate and R is the nozzle radius. Three lines were printed for each ink-nozzle-flow rate combination to study the repeatability. A microscope camera is incorporated to visualize the printing behavior during these experiments as shown in Fig.1.

2.3.2 Geometric Characterization of the Prints (Zygo/Optical)

To quantitatively characterize the geometry of the prints Zygo NewView 6300 3D profilometer with a 50x scan lens was used. Geometric features such as width, height and cross-sectional area were measured to be used in calculations of electrical conductivity detailed in Section 2.5. The cross-section of the printed lines are depicted in Fig 1 (b). As shown, the base width (a) is smaller than the overall width of the lines (b), preventing the profilometry from capturing the base-width detail. To address this issue, base width was measured through optical microscopy (Zeiss Axion 105) images taken from the bottom of the glass slides as shown in the Fig 1 (b). The data obtained from both the equipment is further analyzed using MATLAB program to get an approximated cross-sectional area (A_M) of the printed line.

To consider the porosity of the printed structure various observations were done on the printed structure. Firstly, the solid volume percentage (s) was calculated by weighing and subtracting the ink mass before and after evaporation,and dividing the result by the solid concentration. This was then utilized to calculate the expected cross-sectional area (A_p) of the printed structure after evaporation, which is given by

$$A_p = Q * f * s \quad (15)$$

Finally, the porosity of the printed structure was calculated by,

$$P = \frac{1 - A_p}{A_M} \quad (16)$$

2.3.3 Microstructural Characterization (SEM) of the Prints

Scanning Electron Microscope (SEM, FEI Quanta 200F, ThermoFisher, Courtesy of WSU FMIC) with a 400-1000x zoom, 10-14mm working distance and 10-20kV beam power was used to scan the cross-sectional area of the printed lines to analyze the morphology of the constituents.

2.3.4 Measurement of printed line conductivity

The electric conductivity of the printed lines were characterized using the four-probe Kelvin method to measure the DC resistance across the line using an LCR meter (BK Precision Model 894, 500 kHz). On each line, EGaIn droplets were used as soft electrical contacts to establish robust connection of the equipment with the lines, without damaging them (see Fig 3(h-i)).

Resistance is measured among various lengths on the same line. These resistance measurements are further analyzed using the line transmission method[84] assuming the same cross-sectional area across the line length. Thereafter, the resistance is represented as a linear function of the line length;

$$R = \frac{1}{\sigma A} L + R_c \qquad 17$$

Where R is the resistance, σ is the conductivity of the line, A is the cross-sectional area of the line determined in section 2.3.2 , L is the length of the line, measured using image processing program, and R_c is the contact resistance. The slope of the R-L linear regression is used to calculate the conductivity of the printed line.

2.4 Analysis of the Experimental Data

To understand the influence of the key material and process parameters on the printed structure conductivity, we analyze the experimental data by considering three levels of variables as shown in Fig. 2.

We differentiated the experimental data into compositional parameters (EG, Gr , PEO and Act) where $Act = EG + Gr + PEO$ is the total active material concentration, process parameters (R and $\dot{\gamma}_a$), flow mechanism parameters ($\dot{\gamma}_a^{slip}$, $\dot{\gamma}$ and $\dot{\varepsilon}$), porosity (P) and Conductivity (C). Here, the compositional and process parameters can be considered as process inputs and conductivity can be considered as the process output. Flow mechanism parameters and porosity can be considered as intermediate variables since they are dependent on the process inputs but also can have a direct influence on the conductivity. In fact, we postulate in this study that the intermediate parameters

mechanistically explain how process parameters (R and $\dot{\gamma}_a$) dictate the printed line conductivity.

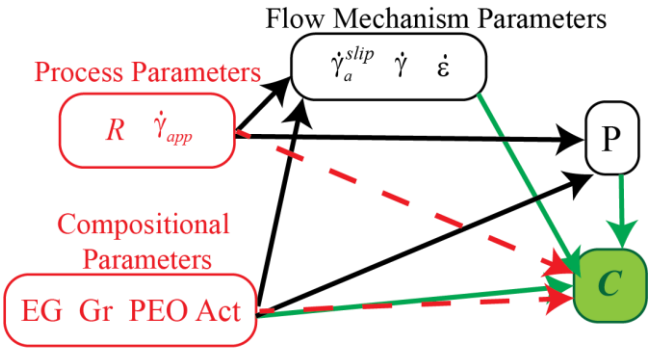

Figure 2. Schematic description of the relationships between various parameters.

It is expected that the material composition will affect the conductivity and porosity through both inherent ways (e.g. generally one would expect increasing the concentration of conductive species will increase the inherent conductivity of the composite) and through processing mechanisms (e.g. increasing the concentration of a given constituent may increase wall slip or shear strain rate, affecting the microstructure of the conductive species thus the resultant conductivity). To capture the former effect, we calculated inherent average conductivity and porosity for each material by averaging these metrics across all printing experiments conducted for that material. Here average conductivity and porosity are given as $C^* = \frac{1}{12}\sum_{i=1}^{12} C_{ik}$ and $P^* = \frac{1}{12}\sum_{i=1}^{12} P_{ik}$, where Cik and Pik are the conductivity and porosity correspond to the experiment i (i.e. specific R-$\dot{\gamma}_a$ combination) for the composition k, respectively. These average quantities provide a measure of the inherent conductivity and porosity for each composition by removing the processing effects. To understand the isolated processing effects, we considered normalized conductivity and porosity given by $\bar{C} = C - C^*$ and $\bar{P} = P - P^*$.

To elucidate how the average and normalized conductivity is influenced by the input and intermediate variables, we employed several analysis techniques. First, stepwise linear regression was performed to obtain models representing the relationships highlighted in Fig.2 between various variable types. These models are summarized below in Eq. 17.

$$\begin{aligned} C^* &\approx g^*(EG, Gr, PEO, Act, P^*) \\ P^* &\approx h^*(EG, Gr, PEO, Act) \\ \bar{C} &\approx f(R, \dot{\gamma}_a, EG, Gr, PEO, Act) \end{aligned} \quad 18$$

$$\bar{C} \approx g\left(\dot{\gamma}_a^{slip}, \dot{\gamma}, P, EG, Gr, PEO, Act\right)$$

$$(\bar{P}, \dot{\gamma}_a^{slip}, \dot{\gamma}, \dot{\varepsilon}) \approx h_i(R, \dot{\gamma}_a, EG, Gr, PEO, Act) \text{ for i= } \bar{P}, \dot{\gamma}_a^{slip}, \dot{\gamma}, \dot{\varepsilon}$$

In addition to this analysis, we also studied the relationship between the compositional parameters and the rheological parameters obtained through capillary and rotational rheometry, and model fitting as follows:

$$(\tau_y, n, K, \beta, m, x) \approx r_i(EG, Gr, PEO, Act) \text{ for i= } \tau_y, n, K, \beta, m, x \qquad 19$$

Details of the stepwise regression process are provided in the supporting information section S2. In each of these models, only the listed input terms and their first order interactions were allowed. The stepwise regression identifies the statistically significant inputs and their interactions as terms in each of the models given in Eq.17. Next, we calculated several statistical quantities to understand the relative importance of these terms. In that, (i) we performed Analysis of Variance (ANOVA) on the data to obtain the Type 3 sum of squares value associated with each term that appear in the regression (SSQ), (ii) we determined standardized regression coefficients by multiplying the regression coefficient of each term with the variance of the term itself and dividing by the variance of the output , (iii) we calculated the partial correlations between each term and the output ($\rho_{partial}$) and, (iv) an importance metric (Im) proposed by Hoffman[85] determined through multiplication of the quantities given in (ii) and (iii). Finally, we calculated the raw correlations for the linear terms to understand the sign of the net effect of the corresponding variable on the output (ρ_{raw}).

3 Results and Discussions

3.1 Capillary Rheometry, Model Fitting and Printing Experiments

Raw pressure vs flow rate data corresponding to two ink compositions, E3.8G10.4P14.2 and E0G10.2P13.9, obtained using the short 250 mm and 600 mm diameter nozzles is shown in Fig.3(a). The dashed curves in this plot are the power law fits to this data, presented along with associated the R2 values, demonstrating that these fits that are used for the rest of the analysis accurately represent the experimental data. Since E0G10.2P13.9 replaces 3.8% EGaIn by volume with acetonitrile, it is expected to exhibit lower viscosity [75], leading it to flow at higher rates at the same pressure levels according to the shear flow theory. The results suggest that this is only true at low flow rates, as the curves converge at high flow rates. This behavior is associated with

the higher prominence of the wall slip behavior with E3.8G10.4P14.2. This is demonstrated through Fig.3 (b) and (c), which show the percent slip and shear contribution values (calculated through Eq 12) for different nozzles and apparent strain rates (high:H, medium:M and low: L), corresponding to E3.8G10.4P14.2 and E0G10.2P13.9, respectively.

Fig 3(d-g) presents the results of the flow model fitting to capillary and rotational rheometry data, respectively for two different ink compositions. In Fig 3 (d) and (f), the circles represent data points generated using the relation given in Eq 4 for various nozzle radii and true wall stress levels within the ranges observed during the experimentation. The curves represent the model fits. Each color circle/ curve corresponds to a different stress level, thus considering the experimentally observed wall stress ranges, higher stress data only correspond to larger nozzle sizes. In general, the model fits accurately represent the

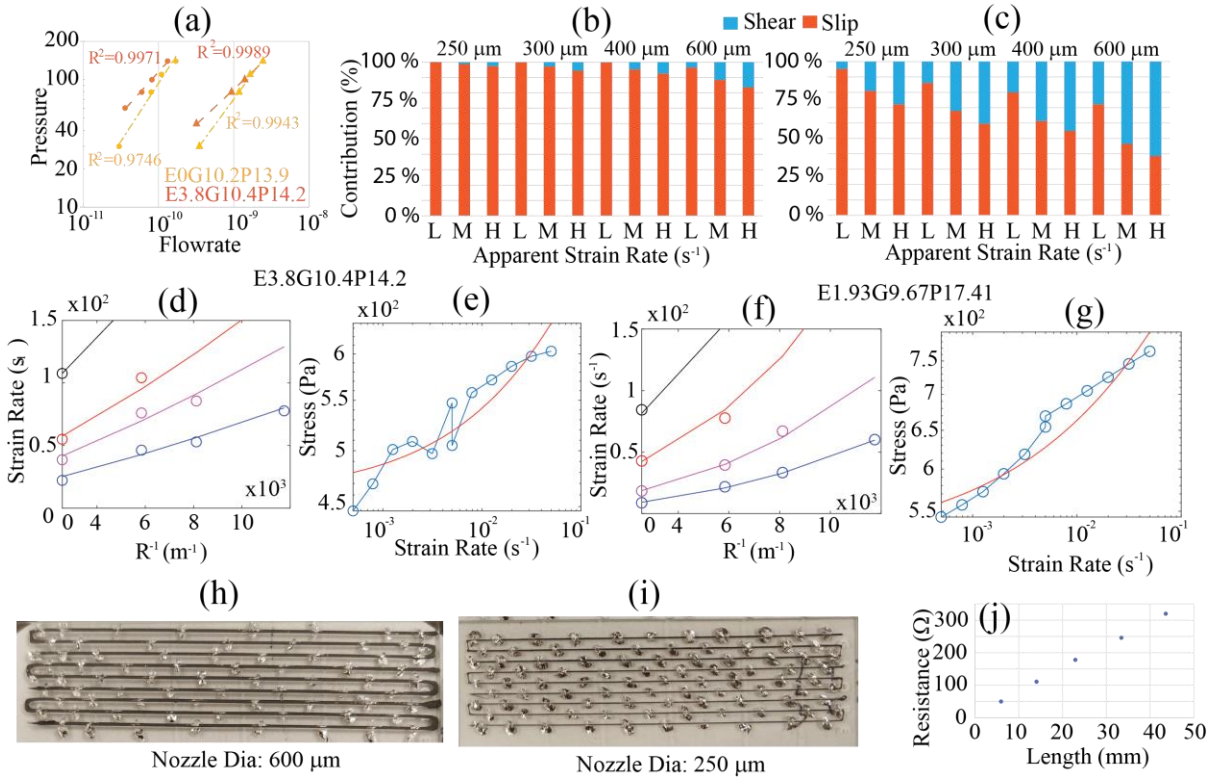

Figure 3. (a) P-Q relations for E3.8G10.4P14.2 and E0G10.2P13.9 featuring nozzle with same radius and two different lengths (b-c) Slip and Shear contributions to the apparent strain rate for inks E3.8G10.4P14.2 and E0G10.2P13.9. (d-g) Flow model fits for two different ink compositions. (h-i) Printed lines using two different nozzle diameters, (j) Sample resistance vs length data for a printed ink.

experimental data as shown. The model parameters for each ink obtained through model fitting is given in Table S2. Results of the statistical analysis of these parameters as a function of compositional variables (Eq 19) revealed only one statistically significant relationship between the total active material concentration and the rate index n as shown in Table 3. Accordingly, the rate index reduces with increasing active material concentration, indicating more active materials lead to a more prominent shear thinning behavior. This is an expected result since shear thinning in polymeric solutions are known to be a product of polymer chain and filler alignment in the flow direction.

Finally, Fig 3(h-i) show the lines printed using 600 and 250 mm diameter nozzles, respectively. Here, the 9 total lines correspond to three apparent strain rates with three repetitions each. The silvery deposits on the lines are the EGaIn droplets placed on the lines following printing and used as electrical contacts during the conductivity measurement. A sample result from line transmission-based conductivity measurement from one of these lines is given in Fig 3(j).

Ink Composition	Average Conductivity (C^*)	Average Porosity (P^*)
E1.8G12.1P13.9	874.2	0.501
E2.9G11.6P14.4	885.0	0.489
E3.8G10.4P14.2	900.9	0.448
E5G10P15	717.4	0.481
E2.6G10.5P17.1	999.0	0.408
E0.5G10.8P17	1230.8	0.458
E1.93G9.67P17.41	1255.8	0.396
E2.9G8.7P17.5	1045.8	0.440
E2G11.2P15.3	864.4	0.478
E0G12P15	954.1	0.529
E0G10.2P13.9	1034.4	0.518

Table 2. Average conductivity and porosities for all inks

3.2 Composition-inherent property relationships

Table 2 lists the average conductivity and porosity for each tested ink composition. The linear regression results for the models given in Eq 18. obtained using this data is provided in Table 3. As shown, electrical conductivity decreases with increasing EGaIn concentration and average porosity with approximately equal importance. This relationship is visually demonstrated in the 3D plot given in Fig 4 (a). The average porosity is inversely dependent on PEO concentration.

Interestingly, the graphene concentration does not seem to have a significant effect on the average ink conductivity.

Term	Coefficient	SSQ	$\rho_{partial}$	Im	ρ_{raw}
$n \approx r_n(EG, Gr, PEO, Act)$					
Act	-0.071	0.139	-0.763	6.250	-0.763
Intercept	2.538				
$C^* \approx g^*(EG, Gr, PEO, Act, P^*)$					
P*	-3008.95	140370.2	-0.887	0.000	-0.483
EG	-86.887	158386	-0.898	0.007	-0.551
Intercept	2572.3				
$P^* \approx h^*(EG, Gr, PEO, Act)$					
PEO	-0.023	0.011	-0.769	20.226	-0.769
Intercept	0.817				

Table 3. Results of the regression analysis for rate index, average conductivity and average porosity

EGaIn particles at these size scales are known to form insulating contacts with other constitutions due to the oxide skin encapsulating the liquid metal [65], [66]. It is accordingly expected for these particles to hinder formation of the conductive graphene networks at the high graphene loading levels and cause reduction in conductivity. Graphene concentration not significantly influencing average conductivity is likely an indication of the tested Graphene concentration range being well above the percolation threshold for this system and not being wide enough to induce a significant conductivity variation. The observed effect of porosity shows that control of porosity becomes an important factor achieving high conductivity and increasing binder concentration is a way to achieve lower porosity.

3.3 Process-driven conductivity analysis

The analysis results detailing the relationships between the process inputs, intermediate variables and normalized conductivity is given in Table 4. The “black-box” analysis between the process inputs and conductivity indicates that the conductivity increases with increasing nozzle radius and

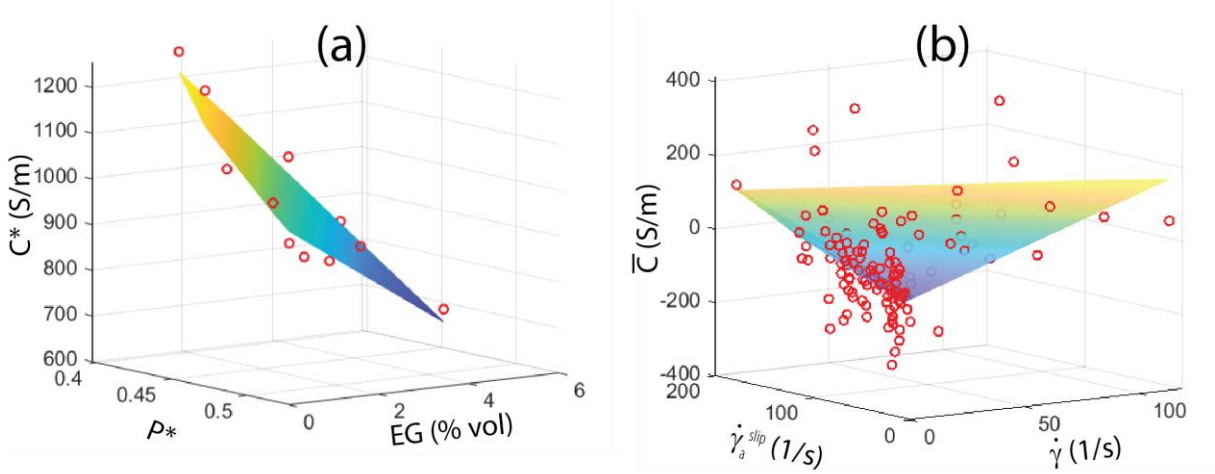

Figure 4. (a) Average conductivity vs EGaIn concentration and average porosity, (b) Normalized conductivity vs $\dot{\gamma}_a^{slip}$ and $\dot{\gamma}$

apparent strain rate, and decreasing total active material concentration as suggested by the raw correlation metric. Various importance metrics calculated suggest that most of the active material concentration effect occurs in the form the interaction with the apparent strain rate, leading to the apparent strain rate having most significant effect on the normalized conductivity. When the relationship between the intermediate variables and normalized conductivity is observed, one could see that both the slip contribution to the apparent strain rate ($\dot{\gamma}_a^{slip}$) and shear strain rate ($\dot{\gamma}$) positively affect the conductivity, with the effect of $\dot{\gamma}$ is being more significant than that of $\dot{\gamma}_a^{slip}$. Additionally, the effect of the process dependent variation of porosity becomes considerable with increasing shear stress as evidenced by the statistically significant interaction terms between these two variables. Figure 4(b) shows all the normalized conductivity values for experimental results as a function of $\dot{\gamma}_a^{slip}$ and $\dot{\gamma}$, along with the plane representing by the linear terms associated with these variables in regression function g. This 3D plot visually demonstrates the correlation of normalized conductivity with these rate terms. Finally, no correlation between the normalized conductivity and extensional strain rate ($\dot{\varepsilon}$) was observed.

The positive correlation between the shear strain rate and conductivity is rather intuitive. Many studies in the literature demonstrated that one or two-dimensional conductive fillers align during DIW along the shear stresses induced inside the nozzles. In this particular case, increasing shear strain rate likely leads to alignment of the graphene platelets along the printing direction,

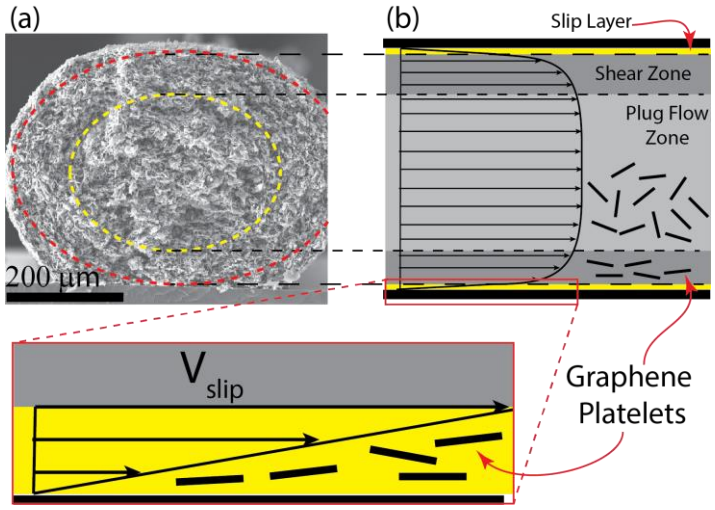

Figure 5. (a) SEM image of a printed filament cross-section, (b) Schematic describing different flow zones inside the nozzles.

facilitating the formation of conductive pathways. The SEM image of a sample filament cross-section shown in Fig.5 highlights a radial alignment pattern within the shear zone where the shear strain rates are non-zero during the flow of a yield-pseudoplastic fluid such as the inks of interest. On the other hand, the positive correlation of conductivity with the slip effects is a non-intuitive observation. Generally, one would expect the increase of slip effects, leading to decrease in shear effects to negatively influence the filler alignment and thus the conductivity in the bulk material. It is possible that the increasing conductivity with the slip effects is associated with the specific wall slip mechanism. It has been reported that one of the prominent wall slip mechanisms during the flow of polymer solutions is the migration of polymer chains from the capillary wall and formation of a low polymer concentration, low viscosity region fluid region, leading significantly high flow velocity gradients near the wall compared to that of the bulk flow[76]. It is possible in this scenario that a similar phenomenon could lead to alignment of graphene flakes under the large strain rates experienced by the solvent rich slip layer near the capillary wall, creating a filament "shell" with high conductivity. The interaction effect between the shear strain rate and the porosity is also expected since the porosity occurs within the core of the filament and its influence on conductivity would only be relevant in cases where the core conductivity is high due to shear alignment of conductive fillers. Finally, it is notable that no ink concentration effects are prevalent in this analysis when the effect of intermediate process variables is considered. Particularly, the

effect of the total active material concentration that is observed in the "black-box" analysis is "absorbed" by the intermediate variables, analysis of which is presented below.

Term	Coefficient	SSQ	$\rho_{partial}$	Im	ρ_{raw}
$\bar{C} \approx f(R, \dot{\gamma}_a, EG, Gr, PEO, Act)$					
R	300000	44200	0.204	0.000	0.167
$\dot{\gamma}_a$	10.231	52438.85	0.221	0.264	0.455
Act	13.567	15564.11	0.123	0.000	-0.056
$\dot{\gamma}_a \times Act$	-0.312	39662.16	-0.193	5.821	
Intercept	-542.040				
$\bar{C} \approx g(\dot{\gamma}_a^{slip}, \dot{\gamma}, \bar{P}, EG, Gr, PEO, Act)$					
$\dot{\gamma}$	1.982	208188.1	0.419	0.032	0.367
$\dot{\gamma}_a^{slip}$	1.024	142278.4	0.357	0.036	0.323
$\bar{P}$	-23.124	62.107	-0.008	0.000	-0.103
$\dot{\gamma} \times \bar{P}$	-56.325	73359.57	-0.264	0.000	
Intercept	-90.829				

Table 4. Results of the regression analysis for the normalized conductivity

3.4 Intermediate variable analysis

Table 5 summarizes the results of the analysis elucidating how the process inputs and ink composition affects the intermediate variables. The shear strain rate is primarily influenced by the apparent strain rate and radius in a positive sense, whereas the total active material and graphene concentration have a negative effect on the shear strain rate. Slip contribution increases with decreasing radius, increasing apparent strain rate, graphene concentration and total active material concentration. The influence of the apparent strain rate is observed to be the most important one as it also amplifies the effect of the other variables, as evidenced by the interaction terms that appear in the regression model. When the importance metrics are examined, the apparent strain rate amplified by the graphene and total active material concentration seems to play a significant role in the overall wall slip. The process dependent porosity variation is a pure function of nozzle radius with increasing radius increasing the porosity. Finally, the extensional strain rate estimates does not show any correlation to the input variables.

The significance of the apparent strain rate to the slip contribution is mathematically intuitive. It has also been shown in the literature that the wall slip effects in cylindrical capillaries generally increase with decreasing radius [78], [86]. It is also expected for increasing solid content, particularly filler particle concentration to lead to increasing slip effects [87]. Since the regression

Term	Coefficient	SSQ	$\rho_{partial}$	Im	ρ_{raw}
$\dot{\gamma} \approx h_{\dot{\gamma}}(R, \dot{\gamma}_a, EG, Gr, PEO, Act)$					
R	113000	6220	0.392	0.000	0.349
$\dot{\gamma}_a$	0.223	8038.845	0.436	0.298	0.398
Act	-2.476	1843.938	-0.226	0.003	-0.133
Gr	-4.854	2696.143	-0.270	0.003	-0.236
Intercept	97.765				
$\dot{\gamma}_a^{slip} \approx h_{\dot{\gamma}_a^{slip}}(R, \dot{\gamma}_a, EG, Gr, PEO, Act)$					
R	-10500	13.1	-0.031	0.0000	-0.170
$\dot{\gamma}_a$	-1.682	779.598	-0.231	0.464	0.910
Act	-1.069	92.240	-0.081	0.000	0.157
Gr	-0.874555	20.61499	-0.03851	0.000	0.008
$R \times \dot{\gamma}_a$	-1246.626	867.7092	-0.24256	0.000	
$Act \times \dot{\gamma}_a$	0.066	1695.479	0.330	21.6	
$Gr \times \dot{\gamma}_a$	0.083	825.483	0.237	2.599	
Intercept	43.336				
$\bar{P} \approx h_{\bar{P}}(R, \dot{\gamma}_a, EG, Gr, PEO)$					
R	169	0.014	0.326	0.000	0.326
Intercept	-0.032				

Table 5. Results of the regression analysis for the intermediate variables

model between these intermediate variables and normalized conductivity (regression model g in Table 4) does not include any significant compositional variables, one could conclude that the negative and positive influence of graphene and total active material composition on shear strain rate and slip effects, effectively cancel each other out within the compositional ranges considered.

It is difficult to reach a definitive conclusion on the influence of EGaIn particle concentration on the intermediate variables using the data available. However, considering that a broader compositional range was examined for EGaIn than that of graphene, one could infer that semi-solid EGaIn particles do not alter the flow mechanisms as much as the more conventional solid fillers.

4. Conclusions

This paper presented an extensive experimental study elucidating the composition-process-property relationships for DIW of graphene-EGaIn-PEO composites. Our results show that the printed structure electrical conductivity is influenced by inherent compositional factors as well as process-driven aspects such as shear flow and wall slip experienced by the inks as well as the porosity of the printed structures. Regarding the former, interesting conclusions can be drawn from the study where EGaIn particle concentration has a negative effect on conductivity, whereas the polymer binder concentration has a positive effect through reduction of the structure porosity. Analysis of the process related effects showed that in addition to the commonly observed shear flow effects on conductive filler alignment and conductivity improvement, wall slip effects were also found to positively influence the printed structure conductivity. Increasing Graphene and total active material concentrations reduced the shear effects while increasing the wall slip effects, leading to a net negative total active material concentration effect on process-driven conductivity, which is primarily driven by the ink flow rate and nozzle radius. Specifically, use of larger nozzles led to increased shear and decreased slip effects, resulting in a net positive influence on printed part conductivity.

On ink design, this works presents a “less is more” perspective by revealing that including higher amounts of active materials, even including conductive fillers, may reduce printed part conductivity, through the influence of ink flow mechanisms and porosity. Specifically, regarding the rather uncommon soft EGaIn fillers, one of the key findings of this study is their inclusion in the composites do not contribute to their inherent conductivity. On the process side, unlike graphene, we have found that EGaIn fillers have a rather neutral effect on shear and slip and thus the associated conductivity variation. These findings draw a different picture compared to some of the earlier studies involving different ink compositions and/or EGaIn particle morphologies.

Our earlier work on similar material systems [60]with significantly lower graphene loadings showed that EGaIn fillers can have a positive contribution to conductivity. Accordingly, we can conclude that increasing graphene loading reduces the contribution of EGaIn fillers to conductivity, rendering them as conductivity inhibitors. In another recent work, Haake et al demonstrated that EGaIn fillers that are an order of magnitude larger than the ones used in this study, can deform and merge under the shear and extensional flows during DIW, forming conducting pathways [69]. Accordingly, this study demonstrates that such effects are not prevalent for EGaIn particles of that are smaller than 5 mm and, in the presence, other rigid fillers.

On process design, the presented results clearly show that higher apparent strain rates lead to high conductivity, most likely due to the shear and slip induced alignment of graphene fillers. This means, at constant nozzle size, higher flow rates and at constant flow rate, lower nozzle sizes are conducive to obtaining higher conductivity. Even though the net isolated effect of increasing nozzle diameter is positive on conductivity, one should note that a statistically significant positive effect of nozzle size on porosity was also observed. Porosity in this context refers to the micro-scale porosity of an individually printed filament. 3D structures consisting of smaller filaments (printed using smaller nozzles) will also exhibit less macro-scale porosity between each filament. Micro and macro-scale porosity will adversely affect printed part integrity and strength and thus should be considered during the process design.

Several limitations of the presented study should be noted. First, the limited number of ink compositions tests provide a limited picture of the effect of the compositional parameters. Second, challenges in flow model fitting in the presence of complex wall slip phenomena have been noted in the literature [80]. In this work, the rotational rheology experiments were run at low strain rate ranges due to the known limitations of the method with highly loaded liquids. This leads to high rate behavior of the inks being only characterized by the capillary rheometry. Expanding the compositional space and incorporating additional rheometry techniques such as squeeze flow can alleviate these concerns, yet come with a significant experimental cost.

This work should be followed and supplemented by several future efforts to maximize its impact. First, detailed microstructural characterization of printed structures is needed to directly observe the morphology of fillers for various ink compositions and process parameters. Second, effect of the ink flow outside the nozzles, during the deposition process on the final part properties should

be studied. In this study, these effects were isolated through using balanced extrusion and a layer height equal to the nozzle diameters. In practice, lower layer heights and higher flow rates are used, inducing higher strain rates experienced by the inks between the nozzle and the substrate. Finally, as the more data is populated using various compositions and processing parameter ranges, emerging data science and machine learning techniques could be utilized to potentially reveal more complex interactions between process inputs and outputs, and realize predictive frameworks for manufacturing parts with as-designed functional properties.

CHAPTER FOUR: NON-LINEAR VISCOELASTIC MODELING OF GR-EG-PEO INK

1. Introduction:

In this chapter, we elucidate our methodology and results in developing a comprehensive model that captures the non-linear viscoelastic behavior of various inks. Our aim is to increase the accuracy of DIW process models by introducing a higher level of sophistication in the material descriptions, especially for intricate material systems. Our objective here is to utilize the shear and extensional rheology of various inks characterized from study 1 to develop complex non-linear viscoelastic constitutive models, which can describe the overall ink behavior during DIW. Through this effort, our goal is to increase the level of sophistication for the material descriptions used in DIW process models to better capture the outcome of the process for such complex material systems.

2. Development of a MATLAB-based viscoelastic constitutive model fitting tool:

Our efforts here involved developing a MATLAB based model fitting tool which is capable of simultaneously fitting shear (shear stress v/s strain rate & normal stress v/s strain rate) and extensional rheology data (transient extensional viscosity v/s strain data) with various non-linear viscoelastic models such as White Metzner (WM), Giesekus, Phan-Thien-Tanner (PTT) and PTT-WM. This tool basically solves the governing constitutive equations of these models under simple shear and extension cases and utilizes a Nelder-Mead Simplex algorithm to fit the models in a least-squares manner.

The data collected from extensional and shear rheology, mentioned in chapter two, are fitted with models using this tool. Firstly, the extensional experiment data measured using

Rheometer and the filament thinning video are analyzed using the MATLAB tool (Extensional_Processing.m in Appendix C). Here, the image processing is performed by converting the RGB frames to grayscale, and the threshold is adjusted to allow for binary image processing techniques. This enables the measurement of the plate diameter in pixel and covert the entire image processing results in meter unit. On this end, we can now measure the changing gap between the plates and the mid-diameter of the filament thinning with respect to time. Subsequently, the video is divided into two parts; the first part is called stretching phase which includes the data when the top plate is in motion and the second phase is called relaxation phase, includes the data after the top plate stops moving. The stretching phase data is then merged with force data collected from the rheometer to determine the extensional viscosity of the ink as a function of Hencky strain. This processing is conducted for four different Hencky strain rates for each ink, and the results are combined using the MATLAB code named PlotMultiRateExtensionalData.m (mentioned in the Appendix C), which saves extensional strain, extensional viscosity, Hencky strain rate, and time in the allextensional.mat file. Secondly, the data from the shear rheology experiment, which includes shear stress, shear strain rate and viscosity and time are further utilized for modeling.

Lastly, univ_fminsearch.m code was used to analyze the data and fit various models using Nelder-Mead Simplex algorithm. This algorithm is designed to accommodate three different inputs; 1. Number of modes: ensuring a more accurate fit. 2. Type of data input, it includes six different options, extensional(ext), flowsweep(FS), flowramp(FR), ext+FS, ext+FR and ext+FS+FR. 3. Type of model, Geiskus, White Metzner, PTT, PTT+WM, PTT+WM+Carreau

Yasuda. Each input plays a crucial role in refining the analysis and ensuring that the models are fitted accurately to the data, catering to the specific requirements of the study.

This algorithm employs MATLAB's fminsearch function to solve non-linear optimization problem and determine model variables that locally minimize the error between the experimental data and the model. This function requires an input of initial guesses for each model variable that will be determined, and a cost function which calculates the model error for each iteration of variables with integrated variable bounding within a physically relevant range. Each fit was repeated multiple times with varying initial guesses to ensure the global minima are achieved.

3. Modeling and verification of viscoelastic behavior of GrEgPEO Inks:

Our initial efforts focused on fitting low-loaded inks that were studied in Study 1. These inks exhibited highly viscoelastic behavior allowing completion of extensional rheometry experiments without filament breakup[88]. It was found that, out of all the models above, PTT-WM could simultaneously fit both shear (shear stress v/s strain rate) and extension data (transient extensional viscosity v/s strain data). The constitutive equation for the PTT-WM model is given by

$$Z(tr\ \tau)\tau + \lambda(\dot{\gamma})\hat{\tau} = 2\eta D \qquad 1$$

Where, $Z = 1 + \frac{\varepsilon\lambda(\dot{\gamma})tr(\tau)}{\eta_0}$, $\hat{\tau\tau} = \frac{d\tau}{dt} - (\nabla v)^T.\tau - \tau.\nabla v$, $D = \frac{1}{2}[\nabla v + (\nabla v)^T$ and τ is stress tensor, λ is relaxation time, $\dot{\gamma}$ is strain rate, $\hat{\tau}$ is upper-convected derivation of τ, η is viscosity, ∇v is gradient of velocity vector and ε is non-linear parameter.

This model requires rate dependent viscosity function which explicitly captures shear thinning nature of the inks. Generally, common viscosity models for shear-thinning materials such as power-law, or Carreau-Yasuda are considered for these functions. In the case of low-loaded inks, close observation of the results of the shear rheology indicated a near-constant viscosity at low strain rates, which can be captured through the Carreau-Yasuda type viscosity function given by

$$\eta = (\eta_0 - \eta_\infty) \times (1 + (k \times \dot{\gamma})^{a\frac{n-1}{a}}) + \eta_\infty \qquad 2$$

Where, k is consistency, n is rate index, a is transition index and $\eta\infty$ is infinity rate viscosity.

This function was accordingly entered into the MATLAB framework. The success of these fits relies on the proper initial guesses for the variables involved. In that, we used the shear stress vs. strain rate data obtained from rotational rheometry and applied a Carreau-Yasuda model fit to it using the in-build analysis tool of the rheometer. The parameters extracted from this fit were used as the initial guesses for the rate dependent viscosity function. The results of these fits are shown in Figure 13.

Throughout our experimentation, we encountered specific challenges while working with high-loaded inks. Firstly, we observed early filament breakup during the stretching phase in the extensional rheometry experiments, which imposed limitations on the fitting success of our models. Secondly, when we employed the Herschel-Bulkley (HB) model instead of the Carreau-Yasuda (CY) model for the variable viscosity term, it too demonstrated limited success. These issues highlight the complexities involved in accurately modeling the behavior

of high-loaded inks and suggest that further refinement of the models or alternative approaches may be required to fully capture the intricate rheological properties of these materials.

In future work, to address the complexities presented by high-loaded inks, it is proposed to broaden the scope of experimental data. Incorporating shear frequency or amplitude sweeps, as well as normal stress measurements, could yield a more comprehensive understanding of the ink behavior. Additionally, employing non-linear viscoelastic characterization methods, such as Large Amplitude Oscillatory Shear (LAOS), may generate data that could lead to models with improved fitting accuracy. These methods have the potential to offer a deeper insight into the viscoelastic properties of the inks, thereby enhancing the predictive capability of our models for the direct-ink-writing process.

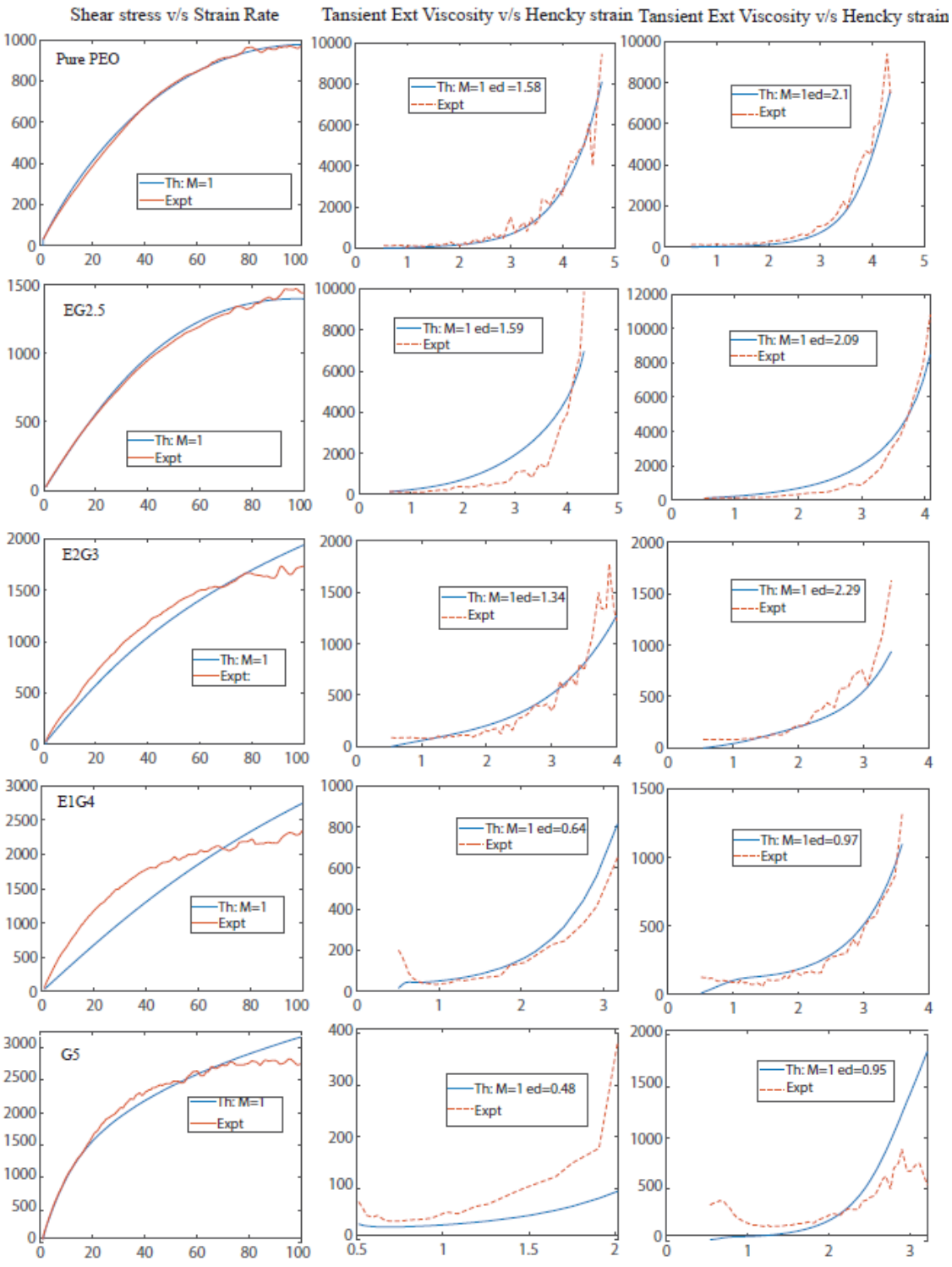

Figure 1. Fitting rheological data of inks mentioned in Study I with PTT-WM model using Carreau-Yasuda viscosity function.

CHAPTER FIVE: CONCLUSIONS AND FUTURE WORK

In this thesis, we have conducted a detailed study of the material-process-property relationships for Direct Ink Writing (DIW) of polymer composites. Our investigation extensively explored the characteristics of solvent-based inks prepared from poly(ethylene oxide) (PEO), graphene, and Eutectic Gallium Indium (EGaIn), tailored specifically for the DIW process. A significant aspect of our research involved examining the process mechanisms of DIW, focusing on how ink behaves both inside and outside the nozzle during the printing process. We investigated two distinct ink formulations: one with a low filler loading containing 5% volumetric filler, where we explored the influence of EGaIn fillers on the composite rheology and it's influences on the flow and deformation of the ink flowing between the nozzle and substrate; and another with a high filler loading containing 11-15% volumetric fillers, where we studied the mechanics of ink flow inside the nozzles, specifically wall-slip and shear deformation exerted by the nozzle-ink interaction. Furthermore, we analyzed the influence of material constituents, the process and flow mechanisms on the electrical conductivity of the final printed part. Lastly, we demonstrated a sophisticated non-linear viscoelastic constitutive model that comprehensively captured the behavior of our inks under various normal and shear stresses.

The first study presented in chapter two, establishes a connection between the ink rheology and printability of inks in the under-extrusion regime. It illustrates that the incorporation of liquid metal fillers within the graphene-PEO composite inks with enhanced viscoelastic properties, significantly improved the processibility of this material system. This material system, when integrated with EGaIn fillers, allows for DIW under a wide array of conditions, including higher printing speeds, lower flow rates, and higher standoff distances, without compromising

printability. Furthermore, inks with EGaIn can endure high extensional strains and viscoelastic thinning, which permits the printing of exceptionally fine filaments, finer than the nozzle diameter, thereby significantly improving the resolution of the printing process. Moreover, the electrical conductivity of these composites strongly depends on the printing process; therefore, the aforementioned EGaIn based precursor capabilities allow for spatial control of conductivity in 3D-printed composites.

The second study in chapter three thoroughly examines how the composition of materials, the printing process, and the properties of the printed structures are interrelated during the DIW of high-loaded graphene-EGaIn-PEO composites. This is achieved through comprehensive modeling of the ink flow inside the nozzles, distinguishing between the contributions of shear flow and wall-slip and identifying how ink composition influences these contributions. It was found that the electrical conductivity is dependent on the materials used, ink flow mechanisms, and the porosity of the structures. The effect of these variables is analyzed to distinguish between inherent and process-driven factors.

Pertaining to the inherent properties, EGaIn particles in the highly loaded ink were found to negatively impact conductivity while the polymer binder improved conductivity by reducing porosity. On the process side, EGaIn exhibits a neutral effect on shear flow and wall-slip, thus leading to variations in conductivity; this behavior differs from those observation in study one. Here we can say that increase in graphene loading, unlike in study one, reduces the contribution of EGaIn fillers to the electrical conductivity.

On the process-driven side, it is shown that both shear flow and wall-slip lead to conductivity increase in the printed structures, likely through facilitating filler alignment through different mechanisms. It was shown that total active material concentration had a net negative effect on

process-driven conductivity, which is rather contradictory to the conventional wisdom of polymer composite design. This can be explained by the negative correlation of the active material concentration with shear strain rate, overcoming its positive correlation with the wall slip as it pertains to conductivity. Same correlations with shear and slip could be drawn for graphene concentration only but these effects seem to cancel each other given that no direct correlation between the graphene concentration and the process-driven conductivity is found. In addition to these compositional findings, use of larger nozzles exhibits an increase in the shear flow effect and reduces the wall-slip effect resulting to net positive effect on the electrical conductivity.

Recognizing the limitations of previous studies which primarily focused on the viscous behavior of inks, we acknowledge the necessity to research deeper into the complex dynamics of DIW processes. This necessitates an exploration beyond traditional viscoelastic models, as the complexities of ink behavior demand a more comprehensive approach. The complex nature of these inks suggests that linear viscoelasticity models may not sufficiently capture their behavior, leading us to the conclusion that a more advanced approach, such as non-linear viscoelastic modeling, is crucial for a thorough understanding. This realization sets the stage for the third study in chapter four, where we take the first step towards advancing material modeling by developing a model capable of effectively fitting both shear and extensional data.. The PTT-WM model, which utilizes the CY viscosity function for low-loaded ink, demonstrated a strong correlation with our experimental observations. For future work, different types of experiments such as normal stress data, amplitude sweep, and shear frequency should be studied to model the high-loaded inks.

Future Work

The future work outlined in this thesis presents several promising directions to enhance our understanding of Direct Ink Writing (DIW) processes and their outcomes.

1. For high-loaded inks, it is critical to extend the viscoelastic modeling framework to incorporate yield stress fluids. This advancement would address the complexities of high-loaded inks and provide a more comprehensive understanding of their behavior during the DIW process. Given the challenges associated with the extensional rheometry of these inks, various other types of shear rheology characterizations should be considered which include LAOS, frequency sweep, normal stress measurements etc.
2. Exploring the behavior of highly loaded inks between the nozzle and the substrate in both balanced and over-extrusion scenarios is necessary. Understanding how these conditions affect the microstructure and properties of the final printed parts will contribute significantly to the optimization of DIW processes and the quality of the resulting products.
3. Further studies are necessary to extend the findings of Studies 1 and 2 to different material types and broader compositional ranges. This expansion would enable a more universal application of the results, facilitating the adaptation of DIW processes across a wider array of materials and applications.
4. A direct evaluation of the printed part microstructure is an essential next step to Study 2. Such an analysis would not only strengthen the findings of this research but also provide more detailed insights into the physical characteristics of the printed parts, thereby solidifying the link between process parameters and material properties.
5. The development of computational models to simulate ink flow and deformation during DIW processes, as stated by the findings of this thesis, would be a significant advancement. These models could help generalize and extend the understanding of the material-process-property relationships, potentially leading to more efficient and predictable DIW processes.

Such an advancement naturally requires establishment of the viscoelastic modeling framework for a broad range of materials.

REFERENCES

[1] B. Itapu and A. Jayatissa, “A Review in Graphene/Polymer Composites,” *Chemical Science International Journal*, vol. 23, no. 3, pp. 1–16, Jul. 2018, doi: 10.9734/CSJI/2018/41031.

[2] S. N. Tripathi, G. S. S. Rao, A. B. Mathur, and R. Jasra, “Polyolefin/graphene nanocomposites: a review,” *RSC Adv*, vol. 7, no. 38, pp. 23615–23632, 2017, doi: 10.1039/C6RA28392F.

[3] H. Guo, R. Lv, and S. Bai, “Recent advances on 3D printing graphene-based composites,” *Nano Materials Science*, vol. 1, no. 2, pp. 101–115, Jun. 2019, doi: 10.1016/j.nanoms.2019.03.003.

[4] Y.-G. Park, H. S. An, J.-Y. Kim, and J.-U. Park, “High-resolution, reconfigurable printing of liquid metals with three-dimensional structures,” *Sci Adv*, vol. 5, no. 6, Jun. 2019, doi: 10.1126/sciadv.aaw2844.

[5] N. W. Solís Pinargote, A. Smirnov, N. Peretyagin, A. Seleznev, and P. Peretyagin, “Direct Ink Writing Technology (3D Printing) of Graphene-Based Ceramic Nanocomposites: A Review,” *Nanomaterials*, vol. 10, no. 7, p. 1300, Jul. 2020, doi: 10.3390/nano10071300.

[6] T. V. Neumann, E. G. Facchine, B. Leonardo, S. Khan, and M. D. Dickey, “Direct write printing of a self-encapsulating liquid metal–silicone composite,” *Soft Matter*, vol. 16, no. 28, pp. 6608–6618, 2020, doi: 10.1039/D0SM00803F.

[7] F. Krisnadi *et al.*, “Directed Assembly of Liquid Metal–Elastomer Conductors for Stretchable and Self-Healing Electronics,” *Advanced Materials*, vol. 32, no. 30, Jul. 2020, doi: 10.1002/adma.202001642.

[8] T. R. Lear, S.-H. Hyun, J. W. Boley, E. L. White, D. H. Thompson, and R. K. Kramer, “Liquid metal particle popping: Macroscale to nanoscale,” *Extreme Mech Lett*, vol. 13, pp. 126–134, May 2017, doi: 10.1016/j.eml.2017.02.009.

[9] S. Nesaei, D. J. Cavanagh, and A. Gozen, “Rheology of liquid metal particle-based polymer composites: A comparative study,” *J Rheol (N Y N Y)*, vol. 63, no. 4, pp. 559–568, Jul. 2019, doi: 10.1122/1.5082662.

[10] M. H. Malakooti, M. R. Bockstaller, K. Matyjaszewski, and C. Majidi, “Liquid metal nanocomposites,” *Nanoscale Adv*, vol. 2, no. 7, pp. 2668–2677, 2020, doi: 10.1039/D0NA00148A.

[11] J. Wang, G. Cai, S. Li, D. Gao, J. Xiong, and P. S. Lee, “Printable Superelastic Conductors with Extreme Stretchability and Robust Cycling Endurance Enabled by

Liquid-Metal Particles," *Advanced Materials*, vol. 30, no. 16, Apr. 2018, doi: 10.1002/adma.201706157.

[12] E. B. Secor, A. B. Cook, C. E. Tabor, and M. C. Hersam, "Wiring up Liquid Metal: Stable and Robust Electrical Contacts Enabled by Printable Graphene Inks," *Adv Electron Mater*, vol. 4, no. 1, Jan. 2018, doi: 10.1002/aelm.201700483.

[13] A. Fassler and C. Majidi, "Liquid-Phase Metal Inclusions for a Conductive Polymer Composite," *Advanced Materials*, vol. 27, no. 11, pp. 1928–1932, Mar. 2015, doi: 10.1002/adma.201405256.

[14] A. B. Dababneh and I. T. Ozbolat, "Bioprinting Technology: A Current State-of-the-Art Review," *Journal of Manufacturing Science and Engineering, Transactions of the ASME*, vol. 136, no. 6, Sep. 2014, doi: 10.1115/1.4028512.

[15] M. Wei, F. Zhang, W. Wang, P. Alexandridis, C. Zhou, and G. Wu, "3D direct writing fabrication of electrodes for electrochemical storage devices," *J Power Sources*, vol. 354, pp. 134–147, 2017, doi: 10.1016/j.jpowsour.2017.04.042.

[16] J. T. Muth *et al.*, "Embedded 3D Printing of Strain Sensors within Highly Stretchable Elastomers," *Advanced Materials*, vol. 26, no. 36, pp. 6307–631, Jun. 2014, doi: 10.1002/adma.201400334.

[17] S. Nesaei, Y. Song, Y. Wang, X. Ruan, A. Gozen, and Y. Lin, "Micro Additive Manufacturing of Glucose Biosensors: A feasibility study," *Anal Chim Acta*, 2018, doi: 10.1016/j.aca.2018.09.012.

[18] T. Chatterjee and R. Krishnamoorti, "Rheology of polymer carbon nanotubes composites," *Soft Matter*, vol. 9, no. 40. pp. 9515–9529, 2013. doi: 10.1039/c3sm51444g.

[19] J. Donnet and A. Vidal, "Carbon black: surface properties and interactions with elastomers," *Advances in Polymer Science*, vol. 76, pp. 103–127, 1986.

[20] X. Sun, H. Sun, H. Li, and H. Peng, "Developing polymer composite materials: Carbon nanotubes or graphene?," *Advanced Materials*, vol. 25, no. 37, pp. 5153–5176, 2013, doi: 10.1002/adma.201301926.

[21] T. H. Seah and M. Pumera, "Platelet graphite nanofibers/soft polymer composites for electrochemical sensing and biosensing," *Sens Actuators B Chem*, vol. 156, no. 1, pp. 79–83, 2011, doi: 10.1016/j.snb.2011.03.075.

[22] Y. Y. Li, L. T. Li, and B. Li, "Direct ink writing of 3-3 piezoelectric composite," *J Alloys Compd*, vol. 620, pp. 125–128, 2015, doi: 10.1016/j.jallcom.2014.09.124.

[23] J. Zhao, A. B. Morgan, and J. D. Harris, "Rheological characterization of polystyrene-clay nanocomposites to compare the degree of exfoliation and dispersion," *Polymer (Guildf)*, vol. 46, no. 20, pp. 8641–8660, 2005, doi: 10.1016/j.polymer.2005.04.038.

[24] M. A. Skylar-Scott, S. Gunasekaran, and J. A. Lewis, “Laser-assisted direct ink writing of planar and 3D metal architectures,” pp. 1–6, 2016, doi: 10.1073/pnas.1525131113.

[25] N. Kazem, M. D. Bartlett, and C. Majidi, “Extreme Toughening of Soft Materials with Liquid Metal,” *Advanced Materials*, vol. 1706594, p. 1706594, 2018, doi: 10.1002/adma.201706594.

[26] J. W. Boley, E. L. White, G. T.-C. Chiu, and R. K. Kramer, “Direct writing of gallium-indium alloy for stretchable electronics,” *Adv Funct Mater*, vol. 24, no. 23, pp. 3501–3507, Feb. 2014, doi: 10.1002/adfm.201303220.

[27] S. Zhu *et al.*, “Ultrastretchable Fibers with Metallic Conductivity Using a Liquid Metal Alloy Core,” *Adv Funct Mater*, vol. 23, no. 18, pp. 2308–2314, May 2013, doi: 10.1002/adfm.201202405.

[28] M. D. Bartlett, N. Kazem, M. J. Powell-palm, X. Huang, and W. Sun, “High thermal conductivity in soft elastomers with elongated liquid metal inclusions,” pp. 3–8, 2017, doi: 10.1073/pnas.1616377114.

[29] J. W. Boley, E. L. White, and R. K. Kramer, “Mechanically sintered gallium-indium nanoparticles,” *Advanced Materials*, vol. 27, no. 14, pp. 2355–2360, 2015, doi: 10.1002/adma.201404790.

[30] T. V. Neumann, E. G. Facchine, B. Leonardo, S. Khan, and M. D. Dickey, “Direct write printing of a self-encapsulating liquid metal-silicone composite,” *Soft Matter*, vol. 16, no. 28, pp. 6608–6618, 2020, doi: 10.1039/d0sm00803f.

[31] J. Wang, G. Cai, S. Li, D. Gao, J. Xiong, and P. S. Lee, “Printable Superelastic Conductors with Extreme Stretchability and Robust Cycling Endurance Enabled by Liquid-Metal Particles,” *Advanced Materials*, vol. 1706157, p. 1706157, 2018, doi: 10.1002/adma.201706157.

[32] R. Guo *et al.*, “Cu-EGaIn enabled stretchable e-skin for interactive electronics and CT assistant localization,” *Mater Horiz*, vol. 7, no. 7, pp. 1845–1853, 2020, doi: 10.1039/c9mh02066g.

[33] R. Tutika, S. H. Zhou, R. E. Napolitano, and M. D. Bartlett, “Mechanical and Functional Tradeoffs in Multiphase Liquid Metal, Solid Particle Soft Composites,” *Adv Funct Mater*, vol. 28, no. 45, pp. 1–13, 2018, doi: 10.1002/adfm.201804336.

[34] Y. Sargolzaeiaval, V. P. Ramesh, T. V Neumann, R. Miles, M. D. Dickey, and M. C. Öztürk, “High Thermal Conductivity Silicone Elastomer Doped with Graphene Nanoplatelets and Eutectic GaIn Liquid Metal Alloy,” *ECS Journal of Solid State Science and Technology*, vol. 8, no. 6, pp. P357–P362, 2019, doi: 10.1149/2.0271906jss.

[35] G. Yun *et al.*, “Liquid Metal Composites with Anisotropic and Unconventional Piezoconductivity,” *Matter*, vol. 3, no. 3, pp. 824–841, 2020, doi: 10.1016/j.matt.2020.05.022.

[36] A. E. Jakus, E. B. Secor, A. L. Rutz, S. W. Jordan, M. C. Hersam, and R. N. Shah, “Three-dimensional printing of high-content graphene scaffolds for electronic and biomedical applications,” *ACS Nano*, vol. 9, no. 4, pp. 4636–4648, 2015, doi: 10.1021/acsnano.5b01179.

[37] Z. Wang and D. Smith, “Rheology Effects on Predicted Fiber Orientation and Elastic Properties in Large Scale Polymer Composite Additive Manufacturing,” *Journal of Composites Science*, vol. 2, no. 1, p. 10, 2018, doi: 10.3390/jcs2010010.

[38] J. C. Majesté, “Rheology and Processing of Polymer Nanocomposites: Theory, Practice, and New Challenges,” in *Rheology and Processing of Polymer Nanocomposites*, 2016, pp. 69–134. doi: 10.1002/9781118969809.ch3.

[39] S. Nesaei, D. J. Cavanagh, and A. Gozen, “Rheology of liquid metal particle-based polymer composites : A comparative study,” *J. Rheol.*, vol. 63, no. 4, pp. 559–568, 2019, doi: 10.1122/1.5082662.

[40] S. Nesaei, M. D. Rock, Y. Wang, M. Kessler, and A. Gozen, “Additive Manufacturing with Conductive, Viscoelastic Polymer Composites: Direct-Ink-Writing of Electrolytic and Anodic Poly(ethylene oxide) Composites,” *Journal of Manufacturing Science and Engineering Additive*, vol. 139, no. c, pp. 1–52, 2017, doi: 10.1115/1.4037238.

[41] M. Nimmakayala and V. R. K. Raju, “Numerical Simulation of Rod-Climbing Effect in Newtonian Fluids,” *Procedia Eng*, vol. 127, pp. 405–412, 2015, doi: 10.1016/j.proeng.2015.11.388.

[42] S. H. Spiegelberg, D. C. Ables, and G. H. McKinley, “The role of end-effects on measurements of extensional viscosity in filament stretching rheometers,” *J Nonnewton Fluid Mech*, vol. 64, no. 2–3, pp. 229–267, 1996, doi: 10.1016/0377-0257(96)01439-5.

[43] H. Yuk and X. Zhao, “A New 3D Printing Strategy by Harnessing Deformation, Instability, and Fracture of Viscoelastic Inks,” *Advanced Materials*, vol. 30, no. 6, pp. 1–8, 2018, doi: 10.1002/adma.201704028.

[44] R. C. Chiechi, E. A. Weiss, M. D. Dickey, and G. M. Whitesides, “Eutectic Gallium–Indium (EGaIn): A Moldable Liquid Metal for Electrical Characterization of Self-Assembled Monolayers,” *Angewandte Chemie*, vol. 120, no. 1, pp. 148–150, Jan. 2008, doi: 10.1002/ange.200703642.

[45] H. B. Harrison, “Obtaining Specific Contact Resistance from Transmission Line Model Measurements,” *IEEE Transactions on Energy Conversion*, vol. 4, no. 2, pp. 160–165, 1989, doi: 10.1109/60.17906.

[46] S. L. Anna and G. H. McKinley, “Elasto-capillary thinning and breakup of model elastic liquids,” *J Rheol (N Y N Y)*, vol. 45, no. 1, p. 115, 2001, doi: 10.1122/1.1332389.

[47] T. R. Lear, S. H. Hyun, J. W. Boley, E. L. White, D. H. Thompson, and R. K. Kramer, “Liquid metal particle popping: Macroscale to nanoscale,” *Extreme Mech Lett*, vol. 13, pp. 126–134, 2017, doi: 10.1016/j.eml.2017.02.009.

[48] G. H. Mckinley, “Visco-Elasto-Capillary Thinning and Break-Up of Complex Fluids,” *Rheology Reviews*, vol. 2005, no. 05, pp. 1–48, 2005, doi: 10.1007/s00247-009-1482-4.

[49] C. Clasen, P. M. Phillips, L. Palangetic, and J. Vermant, “Dispensing of Rheologically Complex Fluids : The Map of Misery,” vol. 58, no. 10, 2012, doi: 10.1002/aic.

[50] R. Rošic, J. Pelipenko, P. Kocbek, S. Baumgartner, M. Bešter-Rogač, and J. Kristl, “The role of rheology of polymer solutions in predicting nanofiber formation by electrospinning,” *Eur Polym J*, vol. 48, no. 8, pp. 1374–1384, 2012, doi: 10.1016/j.eurpolymj.2012.05.001.

[51] A. M. Elliott, O. S. Ivanova, C. B. Williams, and T. A. Campbell, “An investigation of the effects of quantum dot nanoparticles on photopolymer resin for use in polyjet direct 3D printing,” *23rd Annual International Solid Freeform Fabrication Symposium - An Additive Manufacturing Conference, SFF 2012*, no. Section 2, pp. 988–998, 2012.

[52] Y. S. Lipatov and A. E. Feinerman, “The Concentration Dependence of Surface Tension of Polymer Solutions,” *J Adhes*, vol. 3, no. 1, pp. 3–12, 1971, doi: 10.1080/00218467108075001.

[53] L. Friedrich and M. Begley, “Changes in Filament Microstructures During Direct Ink Writing with a Yield Stress Fluid Support,” *ACS Appl Polym Mater*, vol. 2, no. 7, pp. 2528–2540, 2020, doi: 10.1021/acsapm.0c00126.

[54] J. Fukai, H. Ishizuka, Y. Sakai, M. Kaneda, M. Morita, and A. Takahara, “Effects of droplet size and solute concentration on drying process of polymer solution droplets deposited on homogeneous surfaces,” *Int J Heat Mass Transf*, vol. 49, no. 19–20, pp. 3561–3567, 2006, doi: 10.1016/j.ijheatmasstransfer.2006.02.049.

[55] K. Sun, T.-S. Wei, B. Y. Ahn, J. Y. Seo, S. J. Dillon, and J. a Lewis, “3D printing of interdigitated Li-ion microbattery architectures.,” *Adv Mater*, vol. 25, no. 33, pp. 4539–43, Sep. 2013, doi: 10.1002/adma.201301036.

[56] G. Siqueira *et al.*, “Cellulose Nanocrystal Inks for 3D Printing of Textured Cellular Architectures,” *Adv Funct Mater*, vol. 27, no. 12, pp. 1–10, 2017, doi: 10.1002/adfm.201604619.

[57] W. Xu *et al.*, “3D Printing-Enabled Nanoparticle Alignment: A Review of Mechanisms and Applications,” *Small*, vol. 17, no. 45, pp. 1–57, 2021, doi: 10.1002/smll.202100817.

[58] J. P. Lewicki *et al.*, "3D-Printing of Meso-structurally Ordered Carbon Fiber/Polymer Composites with Unprecedented Orthotropic Physical Properties," *Sci Rep*, vol. 7, no. January, p. 43401, 2017, doi: 10.1038/srep43401.

[59] M. L. Shofner, F. J. Rodríguez-Macías, R. Vaidyanathan, and E. V. Barrera, "Single wall nanotube and vapor grown carbon fiber reinforced polymers processed by extrusion freeform fabrication," *Compos Part A Appl Sci Manuf*, vol. 34, no. 12, pp. 1207–1217, 2003, doi: 10.1016/j.compositesa.2003.07.002.

[60] R. Tandel and B. A. Gozen, "Direct-Ink-writing of liquid metal-graphene-based polymer composites: Composition-processing-property relationships," *J Mater Process Technol*, vol. 302, no. September 2021, 2022, doi: 10.1016/j.jmatprotec.2021.117470.

[61] S. Nesaei, M. D. Rock, Y. Wang, M. Kessler, and A. Gozen, "Additive Manufacturing with Conductive, Viscoelastic Polymer Composites: Direct-Ink-Writing of Electrolytic and Anodic Poly(ethylene oxide) Composites," *Journal of Manufacturing Science and Engineering Additive*, vol. 139, no. c, pp. 1–52, 2017, doi: 10.1115/1.4037238.

[62] M. Wei, F. Zhang, W. Wang, P. Alexandridis, C. Zhou, and G. Wu, "3D direct writing fabrication of electrodes for electrochemical storage devices," *J Power Sources*, vol. 354, pp. 134–147, 2017, doi: 10.1016/j.jpowsour.2017.04.042.

[63] M. A. Skylar-Scott, S. Gunasekaran, and J. A. Lewis, "Laser-assisted direct ink writing of planar and 3D metal architectures," pp. 1–6, 2016, doi: 10.1073/pnas.1525131113.

[64] B. Y. Ahn *et al.*, "Omnidirectional printing of flexible, stretchable, and spanning silver microelectrodes.," *Science*, vol. 323, no. 5921, pp. 1590–3, Mar. 2009, doi: 10.1126/science.1168375.

[65] M. G. Mohammed and R. Kramer, "All-Printed Flexible and Stretchable Electronics," *Advanced Materials*, p. 1604965, 2017, doi: 10.1002/adma.201604965.

[66] J. W. Boley, E. L. White, and R. K. Kramer, "Mechanically sintered gallium-indium nanoparticles," *Advanced Materials*, vol. 27, no. 14, pp. 2355–2360, 2015, doi: 10.1002/adma.201404790.

[67] Y. Liu, Q. Wang, S. Bi, W. Zhang, H. Zhou, and X. Jiang, "Water-processable liquid metal nanoparticles by single-step polymer encapsulation," *Nanoscale*, vol. 12, no. 25, pp. 13731–13741, 2020, doi: 10.1039/d0nr00988a.

[68] T. R. Lear, S. H. Hyun, J. W. Boley, E. L. White, D. H. Thompson, and R. K. Kramer, "Liquid metal particle popping: Macroscale to nanoscale," *Extreme Mech Lett*, vol. 13, pp. 126–134, 2017, doi: 10.1016/j.eml.2017.02.009.

[69] A. Haake, R. Tutika, G. M. Schloer, M. D. Bartlett, and E. J. Markvicka, "On-Demand Programming of Liquid Metal-Composite Microstructures through Direct Ink Write 3D Printing," *Advanced Materials*, vol. 34, no. 20, 2022, doi: 10.1002/adma.202200182.

[70] Y. Sargolzaeiaval, V. P. Ramesh, T. V Neumann, R. Miles, M. D. Dickey, and M. C. Öztürk, "High Thermal Conductivity Silicone Elastomer Doped with Graphene Nanoplatelets and Eutectic GaIn Liquid Metal Alloy," *ECS Journal of Solid State Science and Technology*, vol. 8, no. 6, pp. P357–P362, 2019, doi: 10.1149/2.0271906jss.

[71] J. Wang, G. Cai, S. Li, D. Gao, J. Xiong, and P. S. Lee, "Printable Superelastic Conductors with Extreme Stretchability and Robust Cycling Endurance Enabled by Liquid-Metal Particles," *Advanced Materials*, vol. 1706157, p. 1706157, 2018, doi: 10.1002/adma.201706157.

[72] R. Guo *et al.*, "Cu-EGaIn enabled stretchable e-skin for interactive electronics and CT assistant localization," *Mater Horiz*, vol. 7, no. 7, pp. 1845–1853, 2020, doi: 10.1039/c9mh02066g.

[73] R. Tutika, S. H. Zhou, R. E. Napolitano, and M. D. Bartlett, "Mechanical and Functional Tradeoffs in Multiphase Liquid Metal, Solid Particle Soft Composites," *Adv Funct Mater*, vol. 28, no. 45, pp. 1–13, 2018, doi: 10.1002/adfm.201804336.

[74] G. Yun *et al.*, "Liquid Metal Composites with Anisotropic and Unconventional Piezoconductivity," *Matter*, vol. 3, no. 3, pp. 824–841, 2020, doi: 10.1016/j.matt.2020.05.022.

[75] S. Nesaei, D. J. Cavanagh, and A. Gozen, "Rheology of liquid metal particle-based polymer composites : A comparative study," *J. Rheol.*, vol. 63, no. 4, pp. 559–568, 2019, doi: 10.1122/1.5082662.

[76] P. Wilms, J. Wieringa, T. Blijdenstein, K. van Malssen, J. Hinrichs, and R. Kohlus, "On the difficulty of determining the apparent wall slip of highly concentrated suspensions in pressure driven flows: The accuracy of indirect methods and best practice," *J Nonnewton Fluid Mech*, vol. 299, no. November 2021, 2022, doi: 10.1016/j.jnnfm.2021.104694.

[77] P. Wilms, J. Wieringa, T. Blijdenstein, K. van Malssen, and R. Kohlus, "Quantification of shear viscosity and wall slip velocity of highly concentrated suspensions with non-Newtonian matrices in pressure driven flows," *Rheol Acta*, vol. 60, no. 8, pp. 423–437, 2021, doi: 10.1007/s00397-021-01281-5.

[78] K. T. Estelle and B. A. Gozen, "Complex ink flow mechanisms in micro-direct-ink-writing and their implications on flow rate control," *Addit Manuf*, vol. 59, no. July, 2022, doi: 10.1016/j.addma.2022.103183.

[79] G. M. ECCLESTON and N. E. HUDSON, "The Use of a Capillary Rheometer to Determine the Shear and Extensional Flow Behaviour of Nasal Spray Suspensions," *Journal of Pharmacy and Pharmacology*, vol. 52, no. 10, pp. 1223–1232, 2000, doi: 10.1211/0022357001777351.

[80] H. S. Tang and D. M. Kalyon, “Estimation of the parameters of Herschel-Bulkley fluid under wall slip using a combination of capillary and squeeze flow viscometers,” *Rheol Acta*, vol. 43, no. 1, pp. 80–88, 2004, doi: 10.1007/s00397-003-0322-y.

[81] Y. Qian and S. Kawashima, “Distinguishing dynamic and static yield stress of fresh cement mortars through thixotropy,” *Cem Concr Compos*, vol. 86, pp. 288–296, 2018, doi: 10.1016/j.cemconcomp.2017.11.019.

[82] R. H. Byrd, J. C. Gilbert, and J. Nocedal, “A trust region method based on interior point techniques for nonlinear programming,” *Mathematical Programming, Series B*, vol. 89, no. 1, pp. 149–185, 2000, doi: 10.1007/PL00011391.

[83] F. N. Cogswell, “Converging flow of polymer melts in extrusion dies,” *Polym Eng Sci*, vol. 12, no. 1, pp. 64–73, 1972, doi: 10.1002/pen.760120111.

[84] H. B. Harrison, “Obtaining Specific Contact Resistance from Transmission Line Model Measurements,” *IEEE Transactions on Energy Conversion*, vol. 4, no. 2, pp. 160–165, 1989, doi: 10.1109/60.17906.

[85] P. J. Hoffman, “The Paramorphic Representation of Clinical Judgment,” *Psychol Bull*, vol. 57, no. 2, pp. 116–131, 1960, doi: 10.1037/h0045341.

[86] P. Deng, J. Zhang, F. Liu, K. Liu, H. Liu, and L. Zhang, “Shear-induced flow behavior of three polymers in different size dies,” *Journal of Macromolecular Science, Part B: Physics*, vol. 52, no. 5, pp. 651–661, 2013, doi: 10.1080/00222348.2012.720171.

[87] D. M. Kalyon, “Apparent slip and viscoplasticity of concentrated suspensions,” *J Rheol (N Y N Y)*, vol. 49, no. 3, pp. 621–640, 2005, doi: 10.1122/1.1879043.

[88] S. H. Spiegelberg, D. C. Ables, and G. H. McKinley, “The role of end-effects on measurements of extensional viscosity in filament stretching rheometers,” *J Nonnewton Fluid Mech*, vol. 64, no. 2–3, pp. 229–267, Jun. 1996, doi: 10.1016/0377-0257(96)01439-5.

APPENDIX

APPENDIX A: CHAPTER TWO SUPPORTING INFORMATION

S1 Methods

S1.1 Calibration of the Nozzle-Standoff Distance

Accurate control of the nozzle stand-off distance, especially during printing with small nozzles is critical for achieving a successful print. This parameter specifically influences the first layer of multi-layer prints, issues encountered during which can deteriorate subsequent layers. The process followed to achieve this control is schematically described in Fig S1. First, the vertical distance (ΔZ) between the nozzle end and the focal plane of the laser displacement sensor is measured. To this end, the displacement laser is first focused on the top of the force sensor (by moving the sensor vertically until a 0 reading is acquired from the sensor) and record the Z value from the printer software (Z_1). Next, the force sensor is brought under the nozzle and the nozzle is moved towards the piezo sensor in 1 mm steps until it touches. Upon touching, the nozzle stops moving when a force threshold is reached that is detectable by the sensor. At this point the Z value of the printer is again recorded (Z_2). The printing substrate is then moved under the laser sensor such that the laser points to the starting position of the print and another Z value is recorded (Z_3) at the point where the laser is focused. The desired offset for the nozzle from the substrate is manually entered into the software and the final nozzle position is then:

$$N_{pos} = Z_3 + (Z_2 - Z_1) + Offset \quad \textbf{(S2)}$$

The laser is also used to take readings from the printing surface in a matrix pattern and send the point data to a custom LabVIEW code that determines a plane fit for the surface. This fit is then used to make a rotation matrix that is applied to the Gcode of the print so that the surface grade is considered when printing. This way, the desired standoff distance is maintained during the printing process.

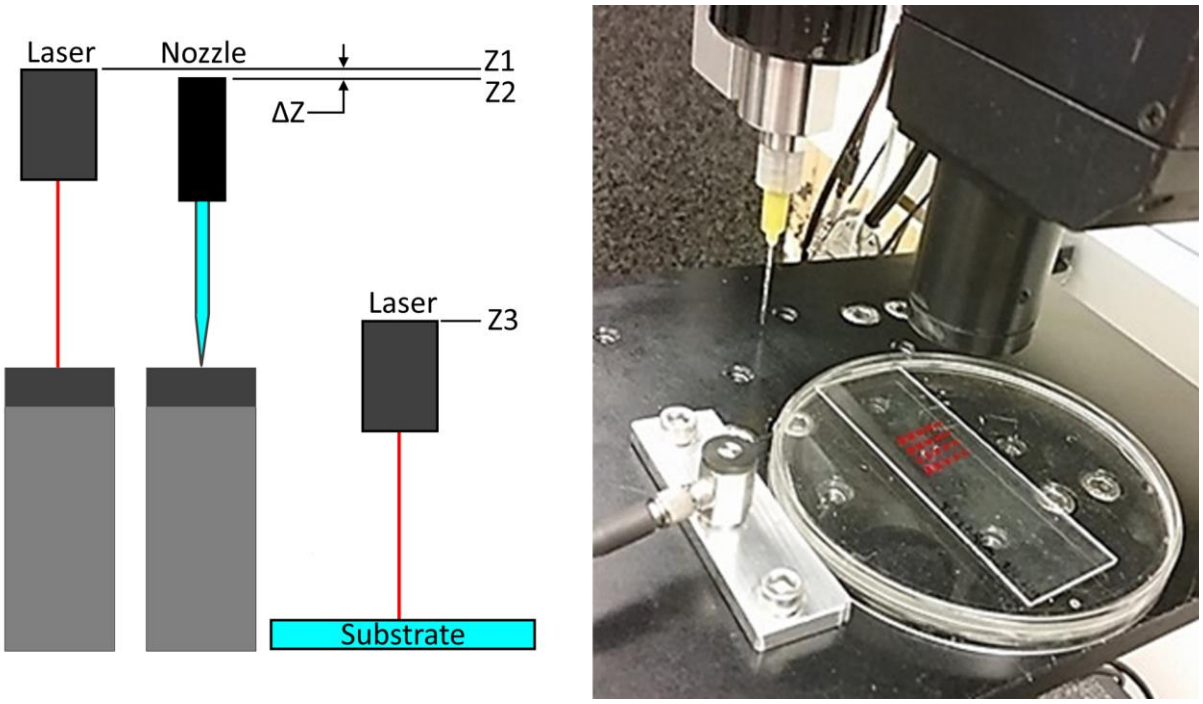

Figure S1: Standoff distance variables (left) and sample picture showing laser interferometer taking multiple points for a plane fit function used while printing (right).

Figure S2: Pictures of the EG2.5 ink stored in syringes

S1.2 Detailed procedure for conductivity measurements

Prior to the electrical characterization of a particular line set (of 3 lines printed under identical conditions), 4 EGaIn droplets were dispensed on the lines such that two of them are on each side of the center point of the line. The two droplets on each side were placed 20 and 25 mm away from the center. The inner droplets were then used as the voltage measurement electrodes while the outer droplets were used as the current injecting electrodes within the Kelvin-probe scheme to collect the data for the line length of 40 mm towards the line transmission measurements. After the resistance data is collected, two additional droplets were placed 5 mm closer to the center on each side and the measurement was repeated using the new droplets as the voltage measurement electrodes and the previous voltage measurement electors as the current injection ones. This procedure is repeated to collect conductivity data with 10 mm length increments. The exact distance between the electrodes were measured optically to ensure accuracy of conductivity measurements. The images of the lines with the EGaIn electrodes are given in Fig S2. The measurements are particularly taken at the center region of the lines to ensure the accuracy of printing speed and its correlation to the conductivity. Towards the end points of the

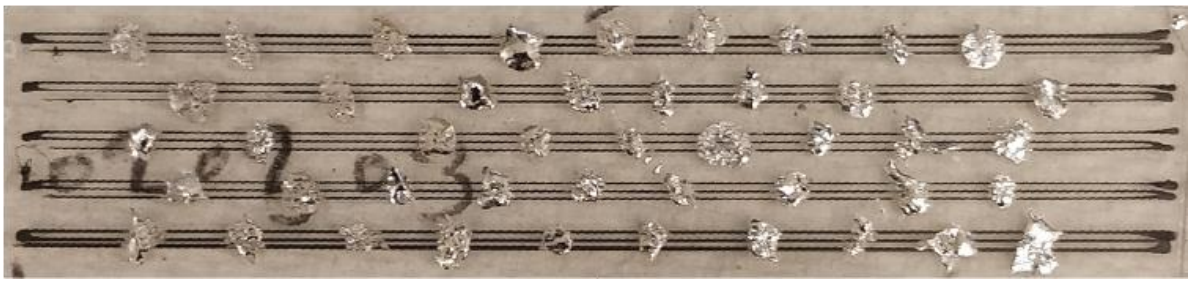

Figure S3: Printed EG2.5 lines with EGaIn electrodes

lines, the positioning stage goes through acceleration and deceleration leading to lower printing speeds locally.

S2 Results

S2.1 Detailed results of the rheological characterization

This section presents the results of shear and extensional rheological characterization corresponding to the inks that were not presented in Section 3.1.

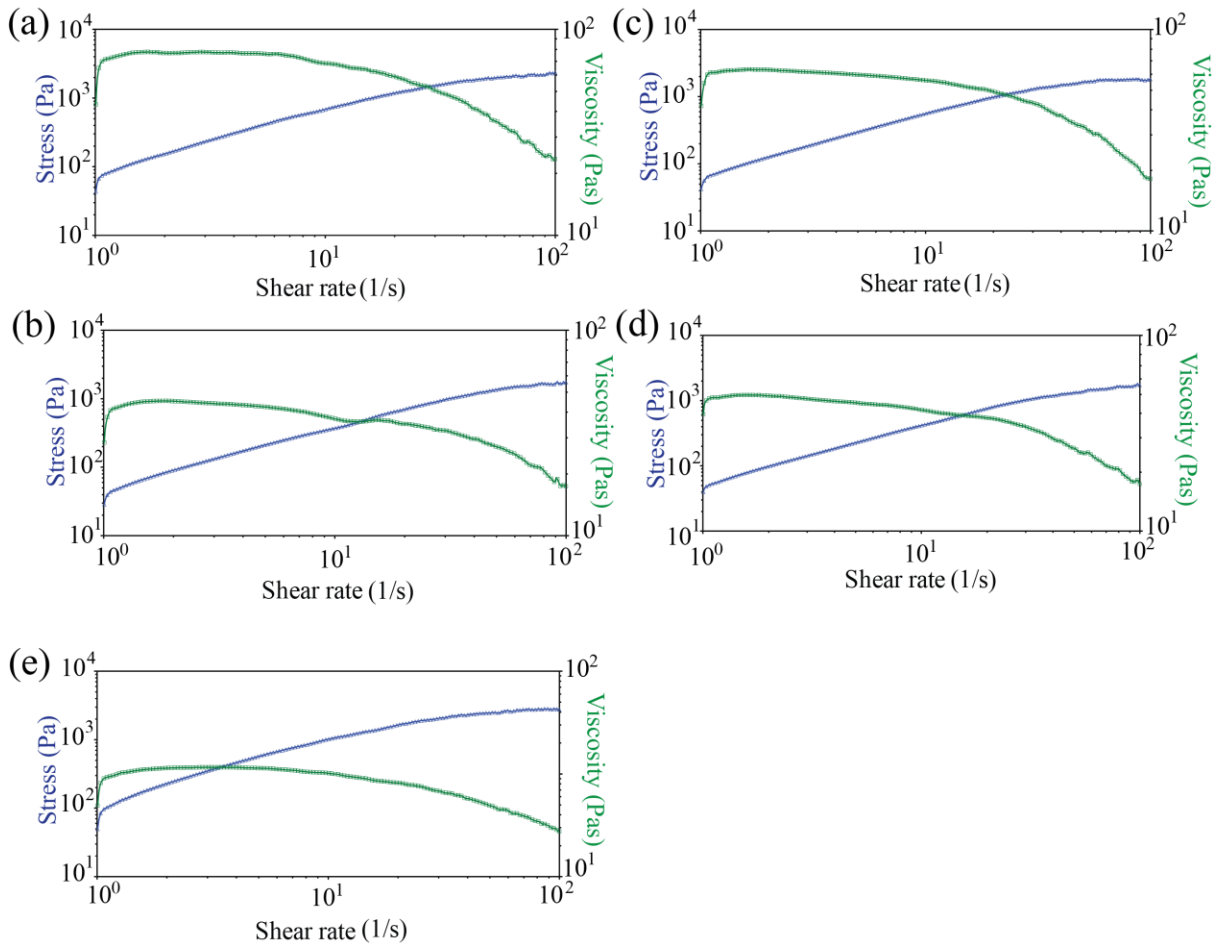

Figure S4: Shear viscosity and stress vs strain data; (a) E1G4, (b) E2G3, (c) G5, (d) G4 and (e) G2.5.

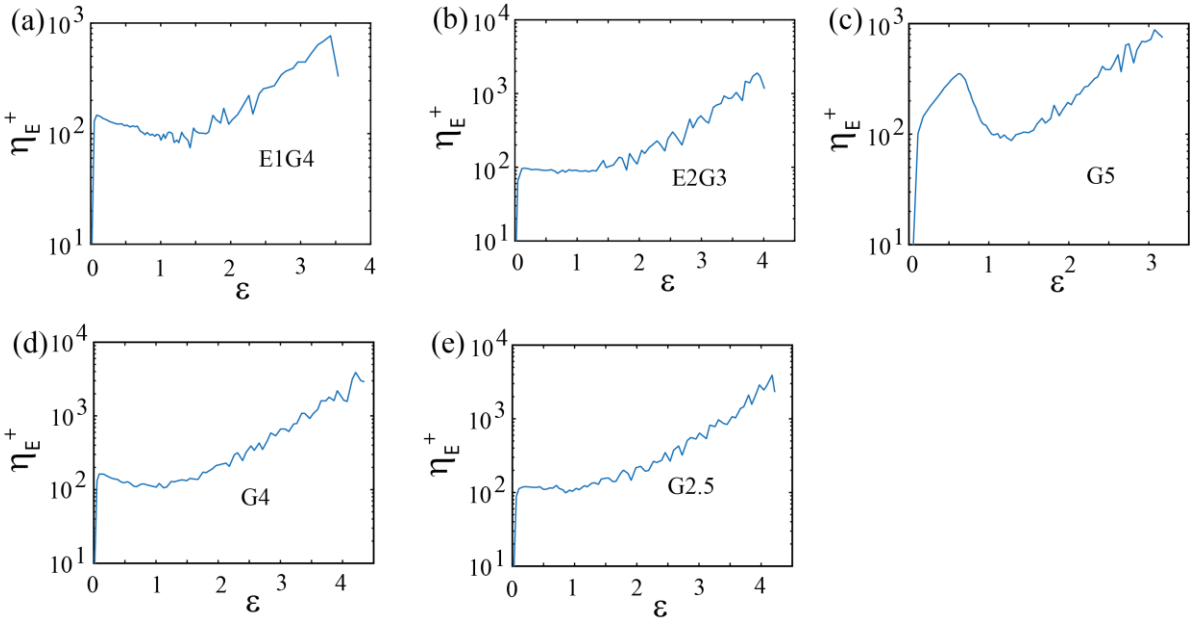

Figure S5: Transient extensional viscosity vs Hencky strain data; (a) E1G4, (b) E2G3, (c) G5, (d) G4 and (e) EG2.5.

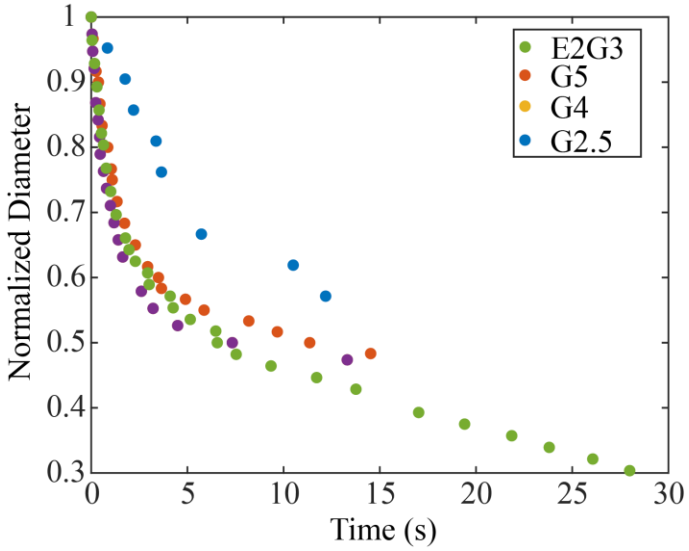

Figure S6. Relaxation profile for the type of inks mentioned in paper.

S2.2 Printing experiments

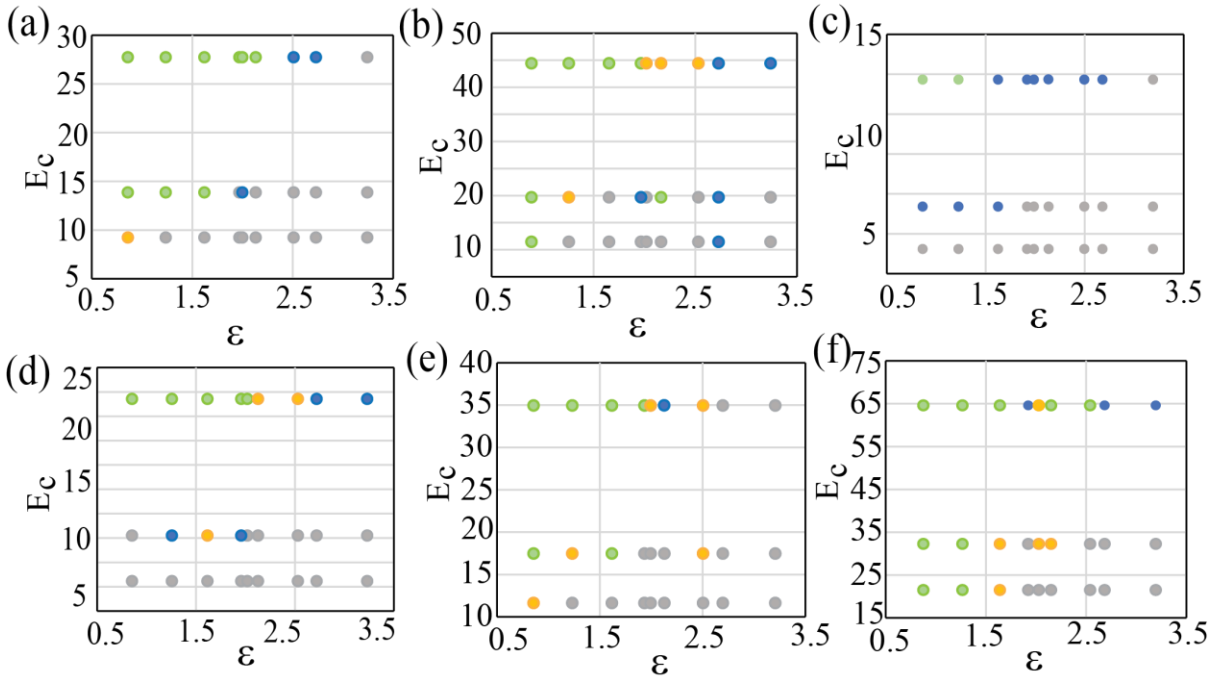

Figure S7: Results of the individual data set of various inks from printing experiments on the Ec-ε plane; (a) E1G4, (b) E2G3, (c) G5, (d) G4 and (e) G2.5 (f) EG2.5

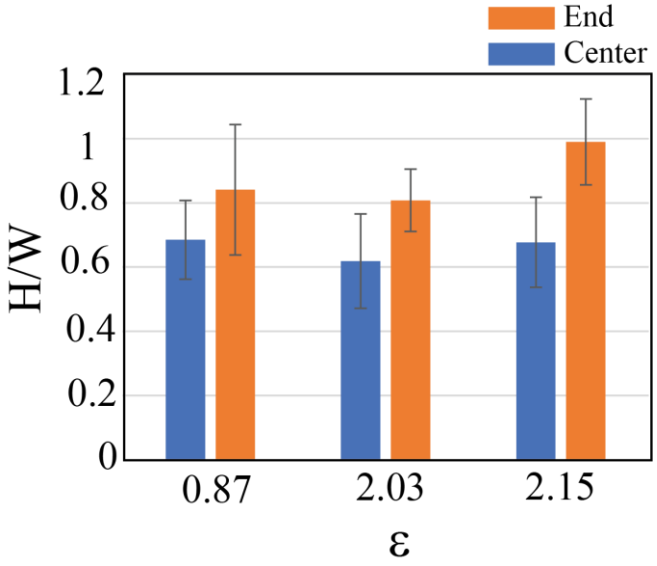

Figure S8: EGaIn particle H/W ratios of the individual center and end points of the printed lines studied in the analysis presented in Figure 8.

APPENDIX B: CHAPTER THREE SUPPORTING INFORMATION

S1. Hybrid Direct-Ink-Write Printhead and Capillary Rheometer System

An in-built direct-ink write printhead with a positive displacement approach was used to 3D print simple serpentine lines. This printer was designed such that it also has capillary rheometry capabilities. Fig. S2 shows the printhead consisting of a non-captive linear stepper motor (SMA-23SN-037062–3.25 V, Helix linear technology) which actuates lead screw with the help of a linear bearing assembly. The lead screw is connected to the syringe piston which dispenses and retracts the ink inside of a 5cc stainless steel syringe (SYR-SS5, New Era Pump System Inc.). A pressure sensor (MFP Flow Plus, ElveFlow) is attached to the nozzle which measures the dispensing pressure in real-time. Teensy microcontroller is used to control this system by running PID feedback loop to maintain desired pressure levels by regulating the piston acceleration. This implementation enables simultaneously monitor the piston velocity and pressure of the system and calculate the flowrate at steady state. A detailed working principle has been described elsewhere [78]

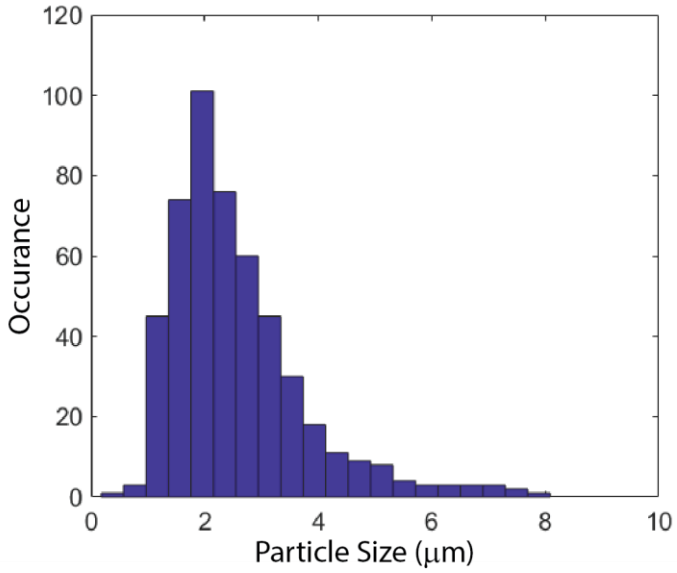

Figure S1 EGaIn particle size distribution

S2. Stepwise Regression Methodology

The stepwise linear regression was performed through MATLABs stepwiselm function. This function starts from an initial linear model correlating the analysis outputs to the inputs and

algorithmically tries to incorporate different model terms while monitoring the p-value for an F-test of the change in the sum of squared error that results from adding or removing each term. A term is added if the p-value for that action is less than 0.05. An existing term is removed if the p-value for that action is greater than 0.1. This procedure continues until the algorithm concludes that no other terms can be added or removed according to this criterion. Only linear terms of each input variables, their pairwise products and a constant term are considered in these regressions. For all the analyses outlined in Eq. 18 and 19, the starting models were selected as the linear combination of the dependent terms which are Act (function of other compositional variables) and all intermediate parameters (functions of process and compositional parameters) whenever applicable. This selection ensures the effect of these dependent inputs is properly captured. Prior to the regressions being performed, outlier data points for each composition were identified using the MATLABs isoutlier function which identifies data points as outliers if the conductivity value for a given data point satisfies $C_{ik} - median(C_k) > -3/(\sqrt{2} \times erfcinv\left(\frac{3}{2}\right))$ where erfcinv is the inverse complimentary error function.

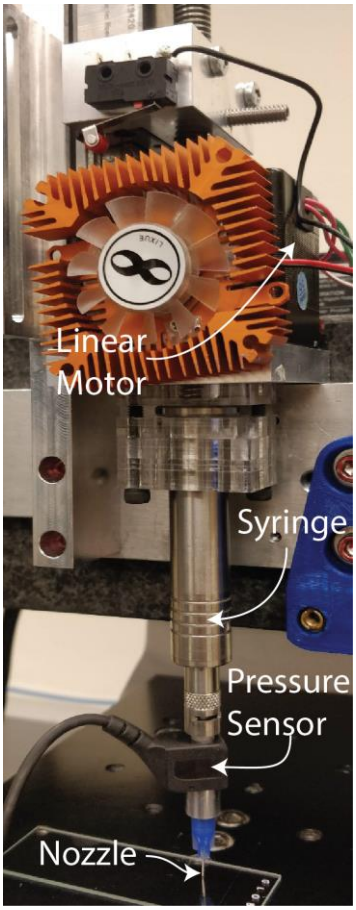

Figure S2 Hybrid direct-ink-writing and capillary rheometry system

Table S1: Exact pressure and apparent strain rate values used during capillary rheometry

	E1.8G12.1P13.9		E2.9G11.6P14.4		E3.8G10.4P14.2		E5G10P15		E2.6G10.5P17.1		E0.5G10.8P17	
R (μm)	$\dot{\gamma}_a$ (s^{-1})	P (psi)	$\dot{\gamma}_a$ (s^{-1})	P (psi)	$\dot{\gamma}_a$ (s^{-1})	P (psi)	$\dot{\gamma}_a$(s^{-1})	P (psi)	$\dot{\gamma}_a$ (s^{-1})	P (psi)	$\dot{\gamma}_a$ (s^{-1})	P (psi)
250	14.55	88	15.73	81.5	20.93	87	18.66	143	17.09	119	9.99	145
	62.31	63.9	51.52	60.5	64.78	61	69.44	100	65.56	83	63.33	98
	104.88	27	66.33	31	116.18	30	120.87	45	110.06	37	111.13	30
300	14.19	76.5	17.94	76	17.22	76.8	20.97	101	16.37	100	12.06	122
	61.72	58.3	47.51	56	61.62	56	67.17	71.7	68.87	76.4	67.75	2.6
	110	26	81.78	32	115.39	26	117.37	35.5	106.82	33.5	107.74	30
400	17.77	71.5	18.22	69	15.95	66.5	19.94	81	19.03	93	13.71	116
	62.97	55	48.15	53.5	64.57	52	66.32	60	66.56	68	64.28	82
	108	29	79.75	31	105.97	25	118.96	30	113.86	33.3	118.65	31
600	16.37	71	18.49	69.5	16.65	67	16.65	72	18.81	92	13.4	108
	58.4	53	48.66	54.5	58.99	50.3	58.99	54.3	69.34	70	63.54	79
	107.24	29.7	80.06	33.5	104.12	26	104	29	110.85	35.2	108.22	32
	E1.93G9.67P17.41		E2.9G8.7P17.5		E2G11.2P15.3		E0G12P15		E0G10.2P13.9			
R (μm)	$\dot{\gamma}_a$ (s^{-1})	P (psi)	$\dot{\gamma}_a$ (s^{-1})	P (psi)	$\dot{\gamma}_a$ (s^{-1})	P (psi)	$\dot{\gamma}_a$(s^{-1})	P (psi)	$\dot{\gamma}_a$ (s^{-1})	P (psi)		
250	10.34	130	15.35	128	109.71	85	14.42	83	17.89	88		
	46.63	90	70.34	89	62.72	59	51.45	58	62.17	60		
	78.37	36	124.31	33	15.74	27	92.86	25	111.57	25		
300	11.03	121	13.31	116	109.71	75	14.36	78	16.39	77		
	45.33	86	62.73	80	62.72	55	55.15	58	60.6	54		
	88.47	36	141.87	30	15.74	26	91.55	25	102.01	22		
400	12.32	107	16.78	96	109.71	70	15.99	70	16.03	74		
	47.08	80	69.85	73	62.72	53	52.58	54.5	65.55	55		
	84.49	36	117.76	30	15.74	27	90.35	27	103.41	22		
600	13.75	107	14.24	90	109.71	73	13.77	67	15.72	79		
	43.71	78	76.01	70	62.72	58	48.68	51	59.23	57		
	83.18	40	112.76	30	15.74	29	83.92	25	96.72	24		

Table S2. The Model fitting parameters obtained for each ink

Ink Composition	Yield stress	Consistency	n	beta	sb	x
E1.8G12.1P13.9	1004.58	2494.80	0.80	9.7e-08	1.34	1.7e-07
E2.9G11.6P14.4	607.05	1166.79	0.53	1.8e-08	1.54	3.3e-06
E3.8G10.4P14.2	460.43	735.10	0.47	3.8e-09	1.38	0.36
E5G10P15	250.78	825.74	0.51	9.8e-09	1.42	0.24
E2.6G10.5P17.1	475.17	1273.11	0.33	4.9e-07	1.09	0.02
E0.5G10.8P17	805.65	1851.57	0.51	8.5e-08	1.30	0.04
E1.93G9.67P17.41	515.20	923.62	0.38	4.8e-15	1.91	1.34
E2.9G8.7P17.5	582.85	596.35	0.44	7.2e-10	0.87	0.94
E2G11.2P15.3	391.56	441.66	0.40	3.8e-11	0.40	1.71
E0G12P15	169.48	288.21	0.60	2.6e-08	0.61	0.87
E0G10.2P13.9	26.72	107.20	0.79	2.6e-06	1.17	1.65

APPENDIX C: CHAPTER FOUR MATLAB CODE

Extensional_Processing.m

```
% Run this to generate indivual Henkey Strain Rate mat file
clc
clear all
close all
global PixelLength;
% Load and read the extensional data and the video
str='H1';
f = readmatrix(strcat(str, '.xlsx'));
save(strcat(str, 'g.mat'), 'f')
v=VideoReader(strcat(str,'.wmv'));
load(strcat(str,'g.mat'));
v.CurrentTime=0; % set the current time to zero
L0=1e-3; %initial gap in m
PixelLength=25e-3/488; % length of a single pixel in m
%% Measure the initial gap and change in mid-filament diameter

dias=[];
gaps=[];
times=[];
dia=1;
while (v.CurrentTime<v.Duration && dia~=0)
im_thresh = imbinarize(rgb2gray(readFrame(v,'native')),0.8); %video processing to adjust
the black and white threshold
im_thresh=imcomplement(im_thresh);
[dia,gap]=MeasureImage(im_thresh); %calling the function
dias=[dias dia*PixelLength]; %save the change in dia
gaps=[gaps gap*PixelLength]; % changing gap
times=[times v.CurrentTime]; %save the time w.r.t.change in dia
drawnow
end
%%
close all
figure
plot(gaps);
pause
xx=ginput(1);%selet the start of gap change
pause
xx=[xx;ginput(1)]; %selet the end of gap change
% merge the data with diameter change and the time
diaArray=dias(ceil(xx(1,1)):floor(xx(2,1)));
timeArray=times(ceil(xx(1,1)):floor(xx(2,1)));
```

```
gapArray=gaps(ceil(xx(1,1)):floor(xx(2,1)));
diaArray2=dias(ceil(xx(2,1)):end);
timeArray2=times(ceil(xx(2,1)):end);
gapArray2=gaps(ceil(xx(2,1)):end);
[diaArray,edotArray]=smoothenDia(timeArray,diaArray);
close all
plot(timeArray,diaArray)
figure
plot(timeArray2,diaArray2)
timeArray=timeArray-timeArray(1); %zero video's initial time
%% merging the experiment data w.r.t cropped video
close all
plot(f(:,3))
pause
xx=ginput(1); %select the start of experiment (change in strain rate)
ind=floor(xx);
ind(1)
ff=f(ind(1):end,:);
ff(:,1)=ff(:,1)-ff(1,1); %zero the time vector for the force
% ff(:,1) and timeArray are all syncronized
ind=find(ff(:,1)<timeArray(end));
fff=interp1(ff(ind,1),-ff(ind,3),timeArray,'linear','extrap');
figure
e(1)=0;
for i=2:length(timeArray)
e(i)=trapz(timeArray(1:i),edotArray(1:i));
end
ar=L0/dias(1)*2;
muext=fff./pi./(diaArray/2).^2./edotArray.*(1+exp(-5*e/3-ar^3)/3/ar^2).^-1;%-
0.04./(diaArray/2)/edot;
semilogy(e,muext);
save(strcat(str,'g.mat'))
figure
plot(ff(ind,1),-ff(ind,3))
hold on
plot(timeArray,fff)
%%
function [dia,gap]=MeasureImage(im_thresh)
global PixelLength;
sz=size(im_thresh);
imshow(im_thresh)
for i=1:sz(1) % find the diameter along the rows for each row
   ind=find(im_thresh(i,:));
   if isempty(ind)
      diaX(i)=0;
```

```
    else
        diaX(i)=abs((ind(1)-ind(end)));
    end
end
hold on


ind=find(diaX>25e-3/PixelLength-22.4); %find the plates in the image
[~,maxind]=max(diff(ind)); % the row at which the top plate ends
gap=abs(ind(maxind)-ind(maxind+1));
minind=(ind(maxind)+ind(maxind+1))/2;
minind=floor(minind); % mid point of the plates
dia=diaX(minind);%get the diameter right there
%below is for visualization
ind2=find(im_thresh(minind,:));

if (diaX~=0)
    plot([ind2(1):ind2(end)],minind*ones(size([ind2(1):ind2(end)])),'r')
end
ind2=find(im_thresh(ind(maxind),:));
plot([ind2(1):ind2(end)],ind(maxind)*ones(size([ind2(1):ind2(end)])),'b')
ind2=find(im_thresh(ind(maxind+1),:));
plot([ind2(1):ind2(end)],ind(maxind+1)*ones(size([ind2(1):ind2(end)])),'b')
end
```

PlotMultiRateExtensionalData.m

```
%load all matfile together to create extensional mat file
clear
% close all
%time=[];
extv=[];

%ed=[];
eps=[];
load H0.5g.mat
clear time
% plot(e,log10(muext),'r');
ind = find(e>0.5);
eps{1} = e(ind);
time{1}=timeArray(ind);
extv{1} = muext(ind);
ed{1}= edotArray(ind);
hold on
load H1g.mat
% plot(e,log10(muext),'r');
```

```
ind = find(e>0.5);
eps{2} = e(ind);
time{2}=timeArray(ind);
extv{2} = muext(ind);
ed{2}= edotArray(ind);
load H1.5g.mat
plot(e,log10(muext),'r');
ind = find(e>0.5);
eps{3} = e(ind);
time{3}=timeArray(ind);
extv{3} = muext(ind);
ed{3}= edotArray(ind);
load H2g.mat
% plot(e,log10(muext),'r');
ind = find(e>0.5);
eps{4} = e(ind);
time{4}=timeArray(ind);
extv{4} = muext(ind);
ed{4}= edotArray(ind);
save allextensional.mat
```

univ_fminsearch.m

```
% Needs PlotMultiRateExtensionalData to be run to generate allextensional.mat
clear all
close all
clc
global e
global ext
global edot
global timeArray
global shearFs
global N1
global gammaD %FlowSweep
global model
global func
global t_shear %time: gD is a function of time.
global gD %flowRamp
global shearFr
global N
global m1
global Nfr
%load, read and assign flowramp data
str='Flowramp';
shearfr = readmatrix(strcat(str, '.xlsx'));
```

```
cutidx = find(shearfr(:,3)>0 & shearfr(:,3)<100);
shearFr = shearfr(cutidx,2);
gD = shearfr(cutidx,3); %strain rate (gamma dot)
t_shear = shearfr(cutidx,1);
Nfr = shearfr(cutidx,4);
%load and assign extensional data.
load allextensional.mat
timeArray = time;
ext = extv; %extensional viscosity
edot = ed; %Henky strain rate
e=eps; % Henky strain
digits(32); %to increase the precision
n=1;  %n=number of modes
type =4;   %1:extensional....2:ext+flowSweep.....3:ext+flowSweep+flowRamp
4:ext+flowRamp 5:FlowSweep 6:FlowRamp
func = @PTT_WM_carreauYasuda;   %@Geiskus(l,alp,mu), @PTT(l,zeta,mu,ep),
@WhiteMetzner(l,k,n), @PTT_WM(G,mu0,k,n,ep)
%boundary conditions
bc = func(0, 0, 0, 0, 0, 'BC');
ms = bc(1,:);
ubs = bc(2,:);
lbs = bc(3,:);
m1 = [];
ub = [];
lb = [];
for i = 1:n %number of loops per mode
m0 = ms;
ub = ubs;
lb = lbs;
init_val = costf(m0, i, type, ub, lb)
options = optimset('Display','iter','PlotFcns',@optimplotfval);
[mf, fval, exitflag] = fminsearch(@(m) costf(m, i, type, ub, lb), m0, options);
m1 = [m1 mf];
s = size(edot);
T12sfs = zeros(1,length(shearFs));
Ns = zeros(1,length(N1));
T12sfr = zeros(length(shearFr),1);
time_fr = [min(t_shear) max(t_shear)]; %time of min and max value of t_shear
for index = 1:s(2)
time = [min(timeArray{index}) max(timeArray{index})];
Ts = zeros(length(timeArray{index}),6);

for j = 1:i
eData{1} = timeArray{index};
eData{2} = edot{index};
```

```
if type<=4
T0 = [10 0 0 0 0 0];
[t, T1] = ode45(@(t,T) func(t, T, eData, m1, j, 'deriv'), time, T0);
T = interp1(t, T1, timeArray{index});
Ts = T + Ts;
end

%FlowSweep
if (type == 2 || type == 3 || type == 5) && (index==1) %index =1 is just to reduce the loop as
shear as only one data set.

y = func(0, 0, 0, m1, j, 'calc_T12');
[T12,N] = deal(y{1}, y{2});
T12sfs = T12 + T12sfs;
Ns = N+Ns;
end

%flowRamp
if (type == 3 || type == 4 || type == 6) && (index==1) %index =1 is just to reduce the loop as
shear as only one data set.
T0 = [28.4 shearFr(1) 0 0 0 0];
[t, T] = ode45(@(t,T) func(t, T, 0, m1, j, 'deriv_shear'), time_fr, T0)
T = interp1(t, T, t_shear);
T12sfr = T(:,2) + T12sfr;
end
end
if type<=4
eev = (Ts(:,1)-Ts(:,2))./eData{2}';
ee{index} = eev';
figure(index+1)
plot(e{index},ee{index},'-', 'DisplayName', ['Th: M=' num2str(i)])
hold on
plot(e{index},ext{index},'--', 'DisplayName', ['Expt_modes till' num2str(i)])
hold on
end

if (type == 2 || type == 3 || type == 5) && (index==1)
figure(s(2)+2)
plot(gammaD,T12sfs','-', 'DisplayName', ['Th: M=' num2str(i) ])
hold on
plot(gammaD,shearFs,'-', 'DisplayName', ['Expt: M=' num2str(i) ])
hold on
figure(s(2)+3)
plot(gammaD,N1,'-', 'DisplayName', ['Th: M=' num2str(i) ])
```

```
hold on
plot(gammaD,Ns','-', 'DisplayName', ['Expt: M=' num2str(i) ])
hold on
% saveas(gcf, ['Gedot_' num2str(eD(1)) '.png'])
end

if (type == 3 || type == 4 || type == 6) && (index==1)
figure(s(2)+4)
plot(gD,T12sfr','-', 'DisplayName', ['Th: M=' num2str(i) ])
hold on
plot(gD,shearFr,'-', 'DisplayName', ['Expt: M=' num2str(i)])
hold on
end
end
end

for index = 1:s(2)
eD = edot{index};
if type<=4
figure(index+1)
legend('show')
saveas(gcf, [char(func) '_Gedot_' num2str(eD(1)) '_M_' num2str(i) '_type_' num2str(type)
'.png'])
end

end

if (type == 2 || type == 3 || type == 5)
figure(s(2)+2)
h=legend('show')
set(h, 'Location', 'best')
saveas(gcf, [char(func) '_FlowSweep_T12_M_' num2str(i) '_type_' num2str(type) '.png'])
figure(s(2)+3)
h=legend('show')
set(h, 'Location', 'best')
saveas(gcf, [char(func) '_FlowSweep_N_M_' num2str(i) '_type_' num2str(type) '.png'])
end

if (type == 3 || type == 4 || type == 6)
figure(s(2)+4)
h=legend('show')
set(h, 'Location', 'best')
saveas(gcf, [char(func) '_FlowRamp_T12_M_' num2str(i) '_type_' num2str(type) '.png'])
end
```

```
save(['Fitting_Result_' char(func) '_type' num2str(type) '_mode' num2str(n)])

%% Cost Function to minimize the error between theoretical and experimental data
% to get vales for l,zeta,mu,ep

function seq=costf(mm, n, type, ub, lb)
global ext
global edot
global gammaD
global timeArray
global shearFs
global N1
global Nfr
global func
global t_shear %time: gD is a function of time.
global gD %flowRamp
global shearFr
global m1

m = [m1 mm];

flag=1;
for i = 1:length(ub)
if m(i)<lb(i) || m(i)>ub(i)
flag = 0;
break;
end
end
if flag == 1
s = size(edot);
Rerr = [];
T12sfs = zeros(1,length(shearFs));
Ns = zeros(1,length(N1));
time_Fr = [min(t_shear) max(t_shear)];
T12sfr = zeros(length(shearFr), 1);
Rs = 0;

for index = 1:s(2)

T0 = [0 0 0 0 0 0];
time = [min(timeArray{index}) max(timeArray{index})];
Ts = zeros(length(timeArray{index}),6);

for j = 1:n
eData{1} = timeArray{index};
```

```
eData{2} = edot{index};
if type<=4

T0 = [0 0 0 0 0 0];

[t, T] = ode45(@(t,T) func(t, T, eData, m, j, 'deriv'), time, T0);
T = interp1(t, T, timeArray{index});
Ts = T + Ts;
end
if (type==2 || type==3 || type==5) && (index==1)
y = func(0, 0, 0,m, j, 'calc_T12');
[T12,N] = deal(y{1}, y{2});
T12sfs = T12 + T12sfs;
Ns = N+Ns;
end

if (type==3 || type==4 || type==6) && (index==1)
T0 = [28.4 0 0 0 0 0];

[t, T] = ode45(@(t,T) func(t, T, 0, m, j, 'deriv_shear'), time_Fr, T0);
T = interp1(t, T, t_shear);
T12sfr = T(:,2) + T12sfr;
end
end

if type<=4
ee{index} = (Ts(:,1)-Ts(:,2))./eData{2}';
err = ee{index}'-ext{index};
Rs = Rs + (sum(err(~isnan(err)).^2)/sum(ext{index}(~isnan(err)).^2))/4;
inf_ee = ~(ext{index}==0);
len = length(ext{index}(inf_ee));
Rerr = [Rerr (ee{index}(inf_ee)'-ext{index}(inf_ee))./(len)];
clear err

end

if (type==3 || type==4 || type==6) && (index == 1)

inf_shear = ~(shearFr==0);
err = (T12sfr(inf_shear)'-shearFr(inf_shear)');
Rs = Rs + sum(err(~isnan(err)).^2)/sum(shearFr(~isnan(err)).^2);
Rerr = [Rerr 1e3*(T12sfr(inf_shear)'-
shearFr(inf_shear)')./(shearFr(inf_shear)')./(length(shearFr(inf_shear)))];
clear err
end
```

```
end
idx = isnan(Rerr);
if length(Rerr(idx))>0.01*length(Rerr)
seq = 1e28;
else
seq=Rs;
end
else
seq = 1e28;
end
end
```